

Article

Comparison of the Shutdown Transitions of the Full-Flow Pump and Axial-Flow Pump

Haifeng Jiao ¹ , Jilian Shan ², Guorui Yang ², Mengcheng Wang ³ and Songshan Chen ^{3,*}

¹ College of Hydraulic Science and Engineering, Yangzhou University, Yangzhou 225000, China

² Shandong Survey and Design Institute of Water Conservancy Co., Ltd., Jinan 250000, China

³ College of Electrical, Energy and Power Engineering, Yangzhou University, Yangzhou 225000, China

* Correspondence: yzcass08@163.com; Tel.: +86-138-1580-8923

Abstract: In this study, a comparative analysis of the shutdown transitions of a full-flow pump and an axial-flow pump was carried out through numerical simulation and model tests. The UDF method was used to achieve control of the impeller rotational speed during shutdown. The results show that during the shutdown transition, the rate of decline of rotational speed, flow rate, and torque of the axial-flow pump are greater than those of the full-flow pump, so the axial-flow pump stops faster than the full-flow pump. The axial force of the axial-flow pump is significantly lower than that of the full-flow pump, and the maximum value of the radial force of the axial-flow pump is approximately 1.14 times that of the full-flow pump. Due to the influence of the clearance backflow vortex, the impeller inlet and outlet of the full-flow pump generate clearance backflow vortices in the near-wall area, resulting in the overall flow pattern of the impeller chamber being worse than that of the axial-flow pump and the hydraulic loss being greater than that of the axial-flow pump. The runaway speed and flow rate of the axial-flow pump are higher than those of the full-flow pump. Due to the influence of the clearance backflow, the range of the high entropy production rate at the suction side of the impeller of the full-flow pump is always larger than that of the axial-flow pump. The research results in this paper can provide theoretical support for the selection and operation of pumps in large low-head pumping stations.

Keywords: full-flow pump; axial-flow pump; shutdown transition; model test; omega vortex; entropy production



Citation: Jiao, H.; Shan, J.; Yang, G.; Wang, M.; Chen, S. Comparison of the Shutdown Transitions of the Full-Flow Pump and Axial-Flow Pump. *J. Mar. Sci. Eng.* **2023**, *11*, 2129. <https://doi.org/10.3390/jmse11112129>

Received: 19 September 2023

Revised: 30 October 2023

Accepted: 6 November 2023

Published: 8 November 2023



Copyright: © 2023 by the authors. Licensee MDPI, Basel, Switzerland. This article is an open access article distributed under the terms and conditions of the Creative Commons Attribution (CC BY) license (<https://creativecommons.org/licenses/by/4.0/>).

1. Introduction

Water transfer projects are widely used to alleviate water scarcity problems in many regions. The full-flow pump (FFP) is typically used in projects where space is limited. The motor of the FFP is installed as a rotor on the impeller shroud, and an S-shaped blade is applied to the FFP, too. The S-shaped blade [1,2], derived from the S-shaped airfoil, is a well-established hydraulic model that is widely used in tidal power generation [3,4], submarine refrigeration systems, pump turbines [5–7], etc. The flow pattern inside the FFP is better because the impeller is driven directly by a motor on its impeller shroud instead of an internal drive shaft. Meanwhile, the flow pattern inside the FFP is more complex under the shutdown transition, which would lead to the instability of the device. Therefore, it is important to study the performance of the FFP under the shutdown transition.

Recently, some studies on the steady characteristics of the FFP have been proposed. Meng et al. [8] found that in an FFP, the backflow clearance causes additional head losses, which reduces the performance of the device. Shi et al. [9–11] showed that in the FFP, backflow causes poorer performance than in the axial-flow pump (AFP). Under design and large flow conditions, the pressure pulsation amplitude of the FFP is smaller than that of the AFP, while under small flow conditions, its pressure pulsation (PP) amplitude is larger than that of the AFP. The above studies show that the stator–rotor clearance (SRC) negatively

affects the flow pattern and performance of the FFP under steady conditions. However, the lack of a method to analyze the flow pattern of the FFP under the shutdown transition makes it difficult. It is worth noting that the structure of the FFP is similar to those of the other hydraulic machines [12,13], such as the AFPs [14,15], the turbines [16–18], and the centrifugal pumps [19–24]. The performance of these hydraulic machines during shutdown transition has been studied extensively. Kan et al. [25,26] carried out numerical simulations to investigate the runaway state of the shaft extension tubular pump. The speed and flow rate decrease with time when the motor is powered off. The pressure pulsation is generated by the water surge, with the main frequency being the impeller passing frequency. Li et al. [27] studied the hydraulic characteristics of a pump-turbine during the shutdown. As the guide vane closes, the torque and flow rate of the unit decreases, and the decrease in speed is closely related to the negative torque on the runner. Ge et al. [28] studied the shutdown transition of centrifugal pumps under large flow condition. They found that the flow rate, torque, and speed changed dramatically during the shutdown transition and finally stabilized at the runaway state. The flow field in the device is very complex, being mainly caused by the change in the flow direction. Zhang et al. [29] experimentally studied the non-inertial stopping transition of centrifugal pumps. It was found that the shorter the stopping time of the centrifugal pump was, the more pronounced the delayed phenomenon of the speed drop at the end of the non-inertial stopping would be.

Meanwhile, some studies on the performance of these hydraulic machines under the start-up transition [30–32] (SUT) have also been proposed. Long et al. [33] researched the SUT of the centrifugal pump using numerical simulation. It was found that in the initial stage of starting, the stall flow rate in the impeller runner is larger, intensifying the rotational stall in the impeller and making the flow more chaotic. Li et al. [34] studied the SUT of a centrifugal pump through numerical simulations. In the early stages of SUT, the transient vortex evolution between the blades is the leading cause of the transient head being below the steady head. Fu et al. [35] investigated the SUT of the AFP through numerical simulations and experiments, using a dynamic grid technique to simulate the vane motion. The transient head is about 1.87 times the rated head when the speed is at the rated speed. The impeller channel is filled with recirculation, flow separation, and vortices. Li et al. [36] researched the SUT of a centrifugal pump using numerical simulation. They found that the delayed dynamic response of the pump was mainly due to the large inertia of the pump and motor. Wang et al. [37] experimentally investigated the SUT of a centrifugal pump. It was found that the motor speed increased linearly when the pump was started at different accelerations and reached its highest value at the end of the SUT. As the starting acceleration increased, the vibration acceleration amplitude increased as the main frequency increased.

In this study, the shutdown transition processes of AFP and FFP were compared using numerical simulations and model tests [38–40]. First, the external characteristics, pressure pulsation, and runaway characteristics of the FFP unit during shutdown transition were tested on the model test bench. Then, the accuracy of calculations was verified by using model tests. Finally, non-constant numerical simulations of the shutdown transition of two pump units were performed, mainly comparing parameters such as rotational speed, flow rate, torque, flow fields, vortices, and entropy production (EP). This work will provide theoretical guidance for the selection of FFPs and AFPs.

2. Numerical Simulation

2.1. Computational Models and Grids

Numerical simulations were carried out for both the AFP and FFP. The three-dimensional (3D) model of the AFP unit consists of six parts: inlet and outlet (I&O) channels, a guide vane (GV), a GV diffusion section, an inlet guide vane (IGV), and impeller. The FFP model has an additional grid of the SRC water body based on the AFP. Both pump devices adopt the SZM35 hydraulic model, and the radii D_1 and D_2 of the impeller hub and shroud are 60 mm and 150 mm, respectively. The number of impeller blades is four, and the hub ratio is 0.4. The

number of GV blades is four, using the diffusion GV type. The number of IGV blades is five, using the straight GV type. The dimension d of the SRC is 1 mm. The speed n is 1421 rpm. The impellers of both the FFP and the AFP are derived from the “S”-shaped hydrofoil, and the relationships between them are shown in Figure 1. Figure 2 shows cross-sectional views of the impeller chambers of the AFP and FFP. As shown in Figure 2, the tip clearance d_1 of the AFP is 0.15 mm and the stator and rotor clearance (SRC) d_2 of the FFP is 1 mm. The red arrow in the figure shows the direction of water flow.

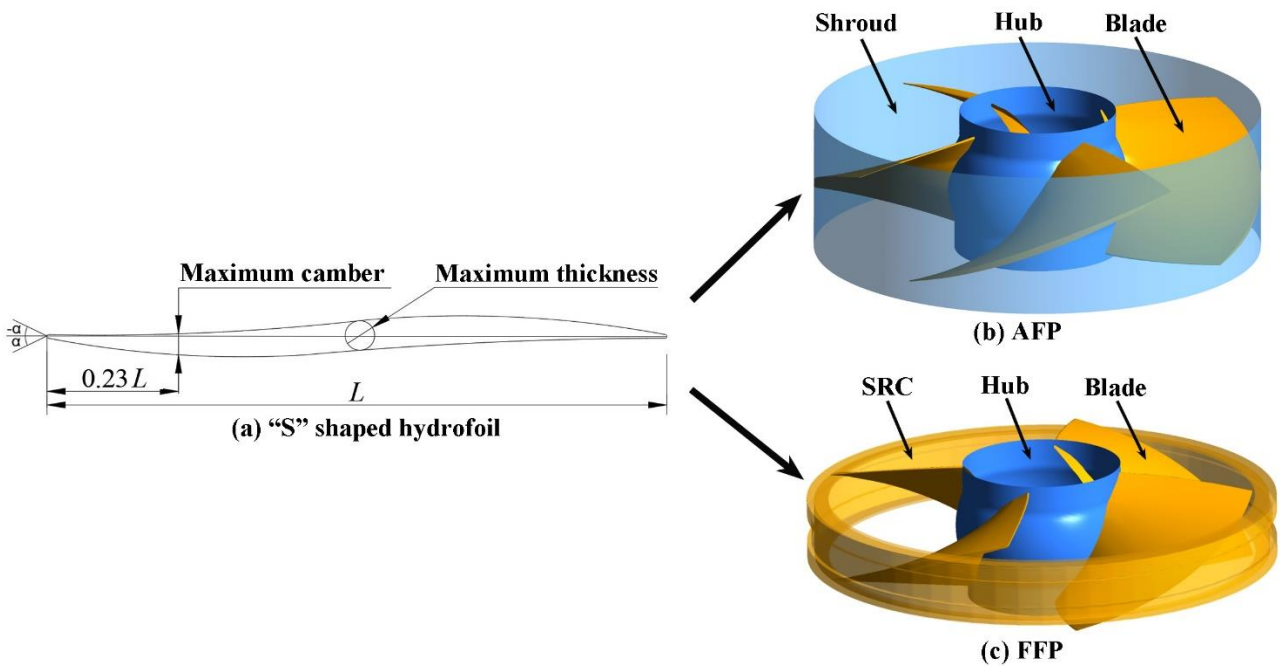


Figure 1. The relationship between the “S”-shaped hydrofoil and the impellers of the AFP and the FFP. (a) two-dimensional schematic of the S-type hydrofoil. (b) impellers of the AFP. (c) Impeller of the FFP.

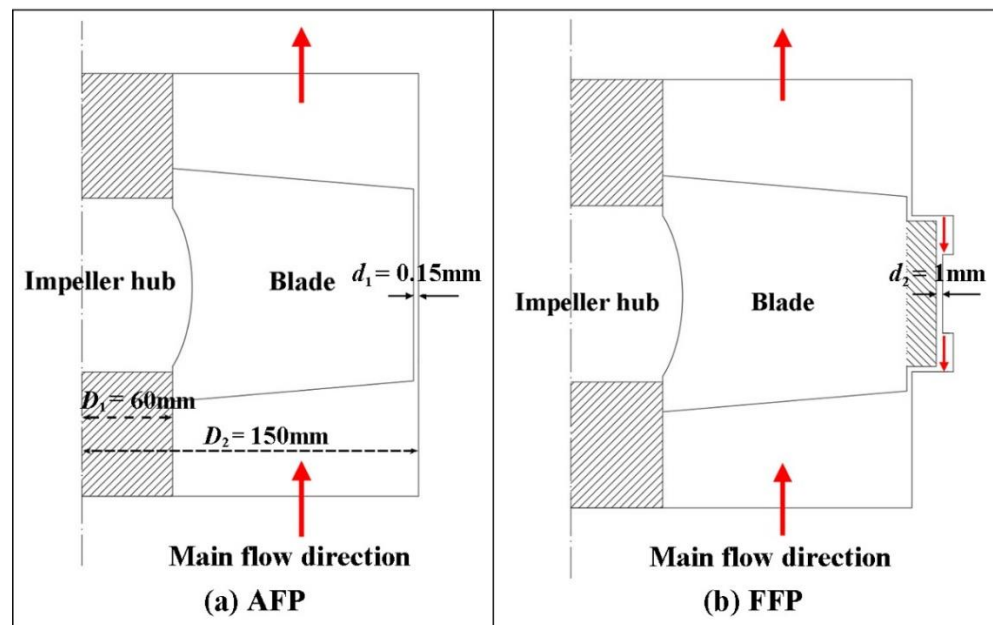


Figure 2. 2D sections of the impeller chambers of the AFP and FFP.

The models of the AFP and FFP differ only in the presence of impellers, and the FFP requires the modeling of the SRC water column. Due to the small SRC size of the FFP, the mesh size near the wall must be carefully considered. The y^+ value is introduced to determine whether the boundary layer grid size meets the computational requirements. According to the research conducted by Zhang et al. [41], the SST $k - \omega$ turbulence model [42,43] requires the value of y^+ to be kept below 50. The distance between the first grid layer and the wall was set to 0.25 mm to simulate the fine flow within the clearance.

A grid-independent analysis of the FFP pump unit model was performed to reduce the influence of the grid on the computational results. As the AFP and FFP models differ only in the impeller area, the independent analysis of the FFP model is also applicable to the AFP. The pump unit characteristics were calculated for the total number of grids in the four scenarios under the design condition, as shown in Figure 3. To control the calculation time and accuracy, both the FFP and AFP use structured grids; their respective grids are 6.91 million and 6.14 million. Table 1 shows the mesh information for each component. Figure 4 shows the 3D computational model of the AFP and FFP devices and the mesh of each part. Figure 5 is a detailed view of the grid.

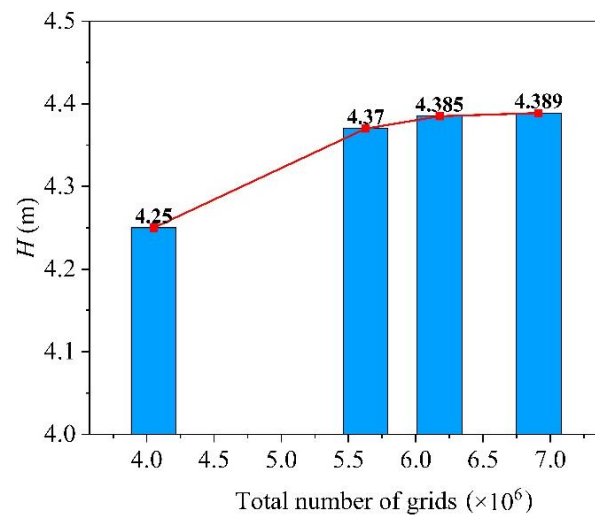


Figure 3. Grid-independent analysis of the FFP.

Table 1. Number of grids in each part of the two pump units.

Part	Grid Type	Node Number	Element Number
IGV	Hexahedral	698,230	652,250
GV	Hexahedral	867,204	806,400
Impeller	Hexahedral	705,600	655,884
Inlet channel	Hexahedral	2,357,676	2,263,757
Outlet channel	Hexahedral	1,391,912	1,358,704
GV diffuser	Hexahedral	411,480	396,981
SRC	Hexahedral	904,032	773,508
Total	Hexahedral	7,336,134	6,907,484

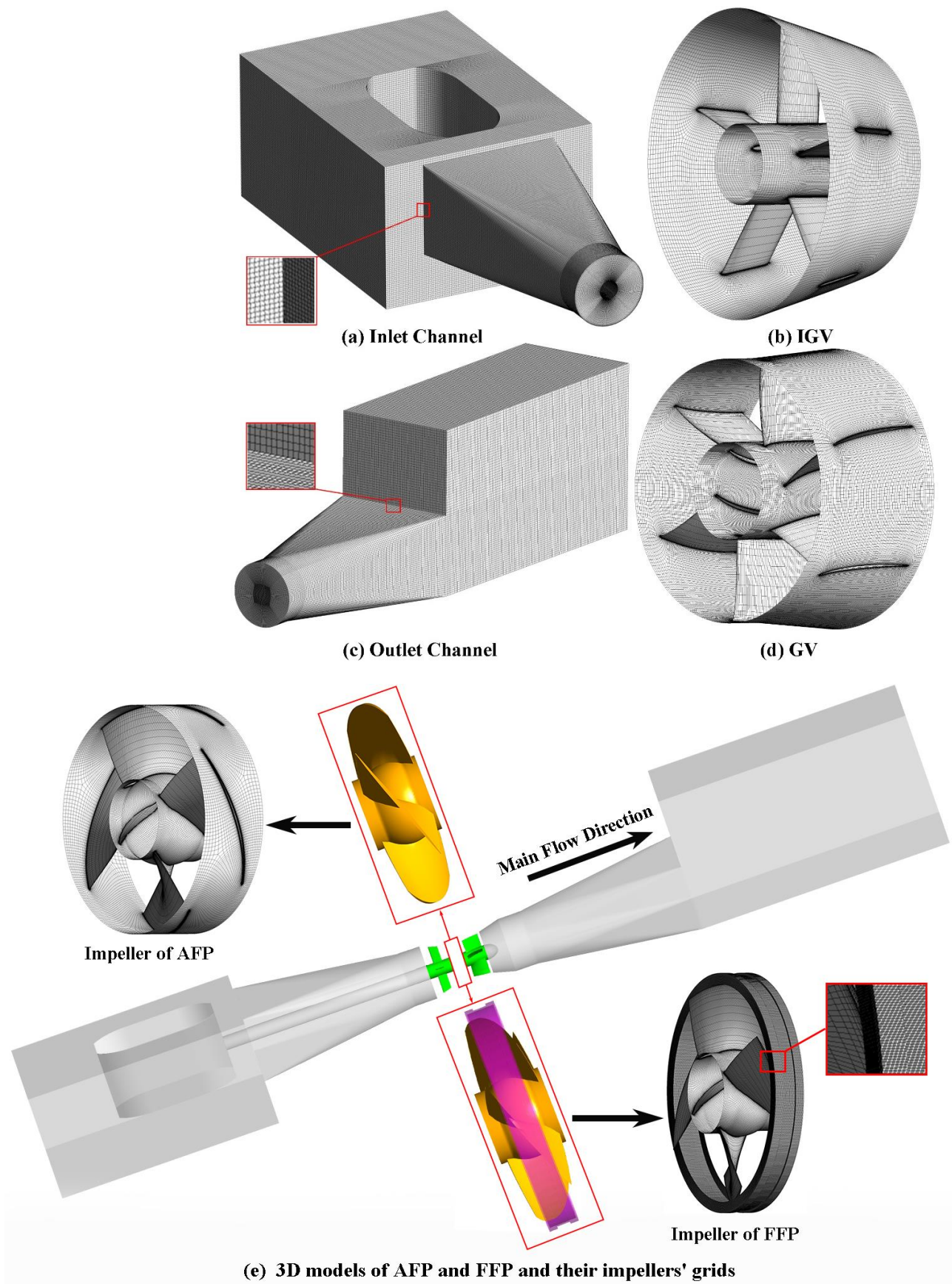


Figure 4. Grids and calculation models.

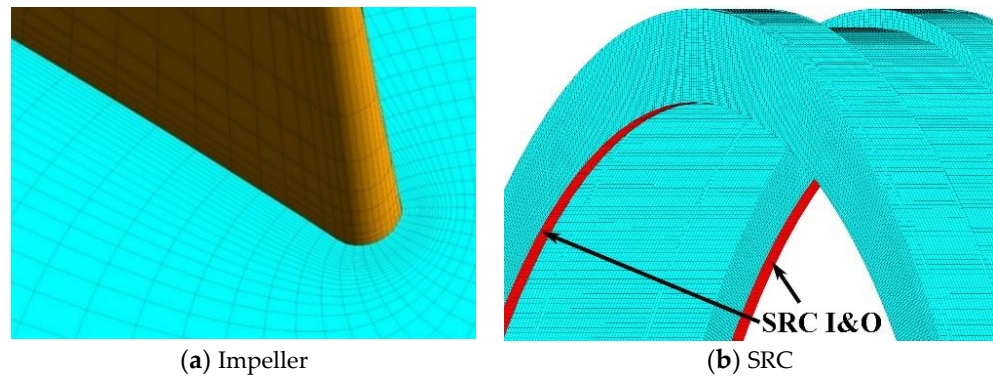


Figure 5. Detailed view of the grid.

2.2. Control Equations

The torque balance equation [44–46] during the shutdown transition of the pump is shown in Equation (1).

$$T_I = T_D - T_W - T_Z - T_R - T_F - T_O \tag{1}$$

Here, T_I is the torque of inertia, T_D is the dragging torque of the motor, T_W is the torque of water, T_Z is the frictional torque of the thrust bearing, T_F is the loss torque of motor fan, T_R is the frictional torque of the radial bearing, and T_O is the oil viscous resistance torque of the thrust head and slip rotor.

The torque of inertia of the rotating parts of the pump unit is calculated as shown in Equation (2).

$$T_I = J_G \frac{d\omega}{dt} = \frac{\pi J}{30} \frac{dn}{dt} \tag{2}$$

Here, ω is the angular velocity, t is the time, J_G is the rotational inertia, and the rotational inertia is calculated to be approximately 0.2 kg/m² for the FFP and 0.18 kg/m² for the AFP.

When T_I is 0, the motor torque is balanced with the sum of the various resistance torques, at which point the pump speed is constant. When the motor is powered off, the motor torque T_D is 0. Equation (1) becomes

$$T_I = -T_W - T_Z - T_F - T_O \tag{3}$$

The viscous oil, frictional, and fan resistances are negligible as they account for a relatively small percentage of the resistance. Equation (3) becomes

$$T_I = J_G \frac{d\omega}{dt} = -T_W \tag{4}$$

The rotational speed during the shutdown transition can be calculated by iterating through Equation (5):

$$\omega_{i+1} = \omega_i + \frac{-T_W}{J_G} dt \tag{5}$$

Here, dt is the time step.

2.3. Algorithm Implementation

The rotational speed and torque of the impeller are key parameters and are central to the study of the shutdown transition. Since the shutdown process of a full-flow pump is a process in which the rotating parts of the pumping unit interact with the water body, etc., it cannot be set up directly in the software and needs to be calculated by using the torque balance equation. Therefore, the rotational speed and torque of the impeller domain are read and loaded via the User-Defined Function (UDF), and the data are output at the end of each step. The UDFs are written in C and loaded to Fluent via compilation to control

the rotational speed of the impeller. At the end of each time step calculation, external characteristics of each parameter are exported and saved in the software. Figure 6 shows the calculation flowchart for the shutdown transition [47].

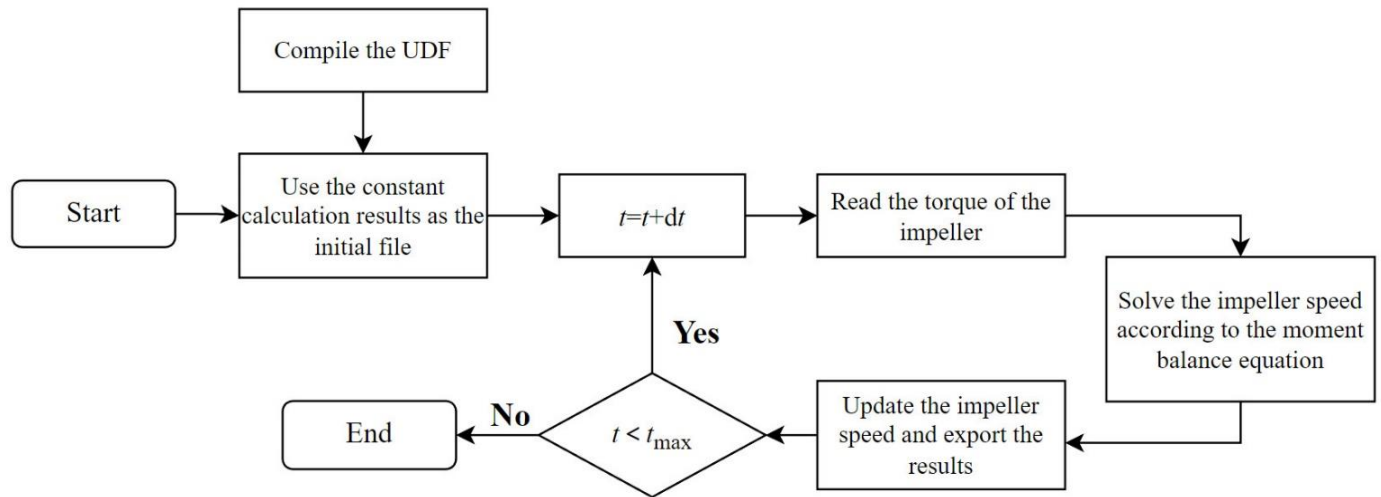


Figure 6. Calculation flowchart for the shutdown transition.

2.4. Boundary Conditions and Calculation Settings

The workstation used for the numerical simulations is equipped with an AMD Ryzen Threadripper 3970X processor with 32 cores, 64 threads, and a frequency of 3.70 GHz. The numerical simulations of the shutdown transition for both FFP and AFP were carried out using the FLUENT 2019R3. The results of the steady-state calculations must be used as the initial flow field before the shutdown transition is calculated. The outlet is set to the total pressure at the corresponding operating conditions. The inlet is set to the static pressure. The impeller domain is set to frame motion, and the impeller blades are set to moving wall. The time step is set to 0.02 s due to computational resource constraints, with 20 iterations in a single time step and a total computation time of 16 s.

3. Model Test

3.1. Introduction to the Test Bench

The tests of the FFP were conducted on the hydro-mechanical test bench at Yangzhou University. The test stand comprises four major parts: hydraulic circulation, power, control, and measurement systems. Like the computational model, the model test pump unit also consists of seven parts. Due to the complex structure of the FFP model, the processing and installation of the rotor motor are difficult. Therefore, an external motor is still used to provide power. Figure 7 is a flow chart of the machining process of the impeller of the FFP. The FFP uses SZM35 impellers machined from SZM35 hydrofoil and made of brass. The rotor material is plastic steel installed on the impeller shroud, as shown in Figure 7c. The IGV and GV are made of stainless steel, and their respective numbers of blades and blade shapes are identical to those in the computational model. Figure 8a shows a 3D schematic of the test bench. Figure 8b shows the physical test bench. Figure 8c is the casing of the impeller chamber.

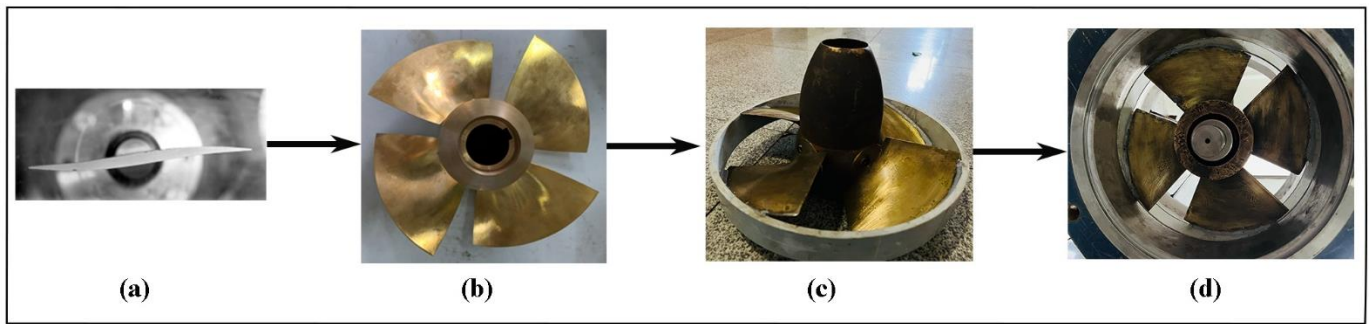
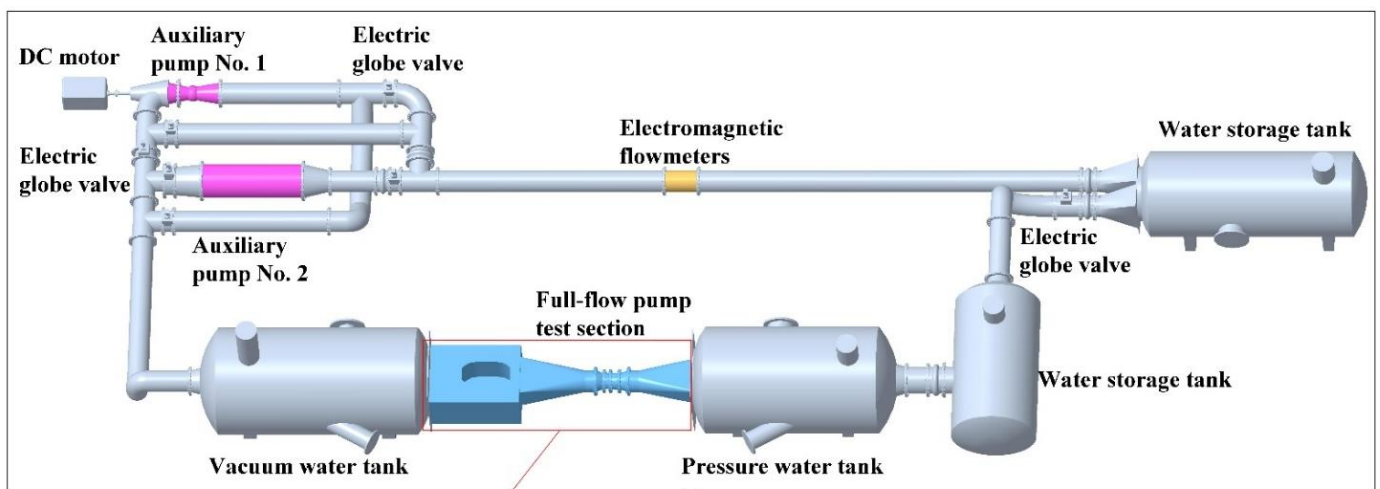
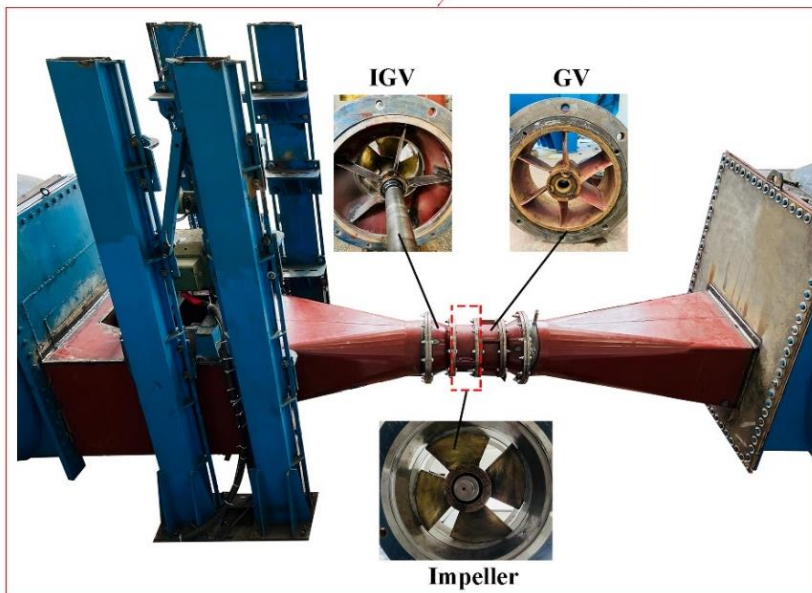


Figure 7. Processing flow of the impeller model of the FFP: (a) SZM35 hydrofoil; (b) SZM35 impeller model; (c) rotor of the FFP; (d) assembly diagram of the impeller of the FFP.



(a)



(b)



(c)

Figure 8. Test device: (a) test system; (b) physical test bench; (c) housing of the impeller chamber of the FFP.

3.2. Verification of the Accuracy of the Calculation

3.2.1. Verification of External Characteristics

The constant external properties of the FFP can verify the accuracy of the computational model, so external properties tests were carried out on the FFP. Figure 9 shows a comparison of the experimental and calculated head curves. The flow coefficient Q_c and the head coefficient H_c are calculated using Equations (6) and (7), respectively [48,49].

$$Q_c = \frac{Q}{Q_d} \tag{6}$$

$$H_c = \frac{H}{H_d} \tag{7}$$

Here, Q is the mass flow rate, H is the head, Q_d is the design flow rate, and H_d is the design head.

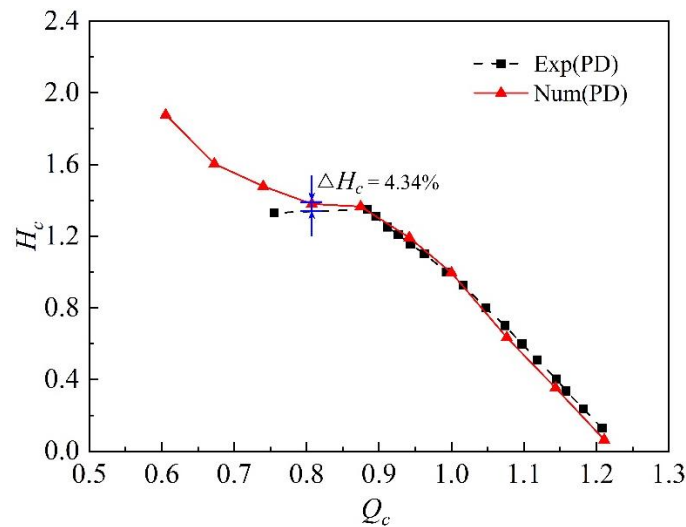


Figure 9. Comparison of head curves of FFP.

The results in Figure 9 show that the H_c of the numerical calculation (Num) and the experiment (Exp) are in good agreement at high flow rates, and the deviation is relatively large at a small flow rate. However, the total deviation is less than 5%. The external-characteristic experiment shows that the computational model is accurate and credible.

3.2.2. Verification of Transient Characteristics

As the shutdown transition is a transient process, the accuracy of transient simulations could be verified by testing the runaway characteristics and PP characteristics. The runaway speed of FFP was tested using a model test. Figure 10a shows that both the calculated and experimental runaway rotational speeds n_r increase with the increase in the head difference. The difference between the simulated and experimental n_r increases as the H increases. The maximum difference Δn_r between the experimental and numerical simulations of the runaway speed of the FFP is approximately 32.5 rpm; this deviation accounts for approximately 3.21%, which is within the normal range. The experimental results are smaller than the calculated results. This is because losses such as the viscous torque of the oil are neglected in the numerical simulations.

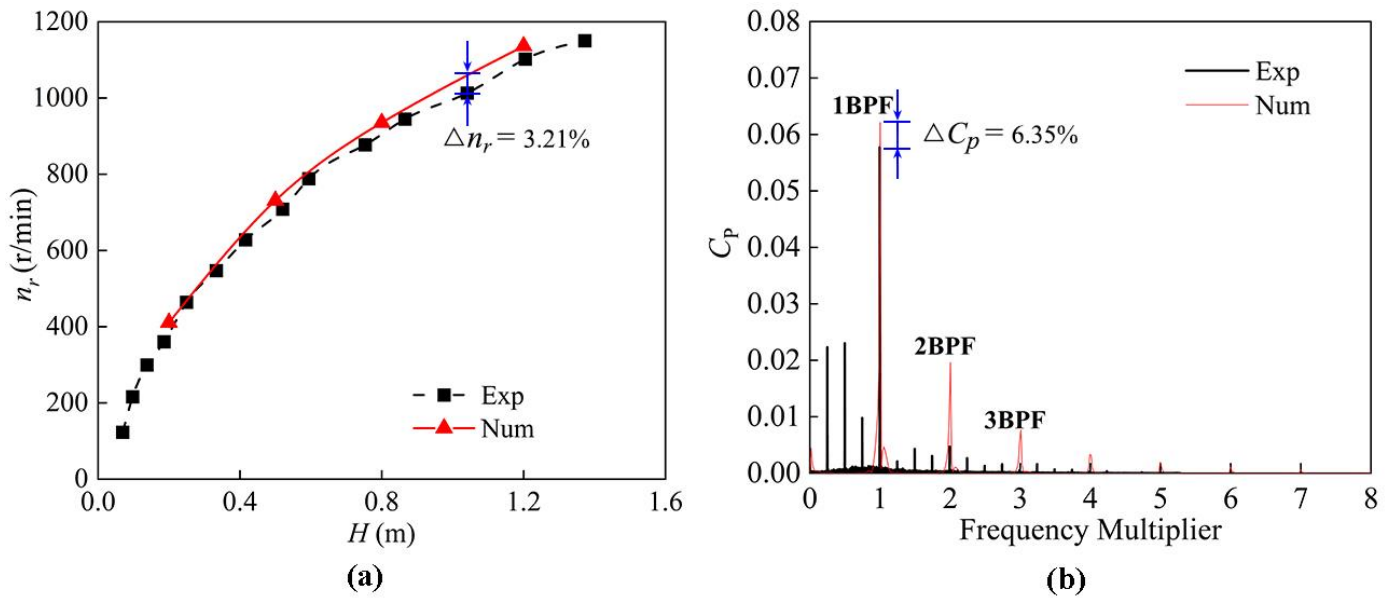


Figure 10. Verification of transient result for FFP: (a) runaway characteristics and (b) PP characteristics.

The pressure pulsation monitoring point is located at the impeller inlet, and the pressure pulsation time-domain diagram is firstly taken out; then, the frequency-domain characteristics can be derived from the fast Fourier transform of the time-domain characteristics. The PP coefficient [50] C_p is introduced to analyze the PP characteristics, and its formula is

$$C_p = \frac{P - \bar{P}}{0.5\rho u^2} \tag{8}$$

where ρ represents the liquid density, u represents the circumferential velocity, P represents the transient pressure, and \bar{P} represents the average pressure.

Figure 10b compares the frequency domain characteristics of the PP of the impeller inlet between simulation and experiment. The position of the main frequency in the experiment was in agreement with the calculated result. The difference in magnitude ΔC_p between the PP experiment and the calculated results at the main frequency was approximately 0.004, which was a small error. In general, the deviation between the experimental and simulated runaway characteristics and PP characteristics was small, so the calculations of the shutdown transition characteristics could be considered accurate.

4. Results and Discussion

4.1. Steady Characteristics

Before studying the shutdown transition, the performance difference between the AFP and FFP during steady operation was first investigated. The head H and efficiency η curves of AFP and FFP were compared, as shown in Figure 11. It can be seen that the AFP and the FFP had the same trend of change in external characteristics. The H and η of the AFP in steady operation were significantly higher than those of the FFP, in which the H difference between the two pump units was about 1.59 m, and the efficiency difference was about 4.68% under the design condition. The maximum operating efficiency of the AFP in operation was 65.37% and that of the FFP was 59.74%, and the η difference was about 5.63%.

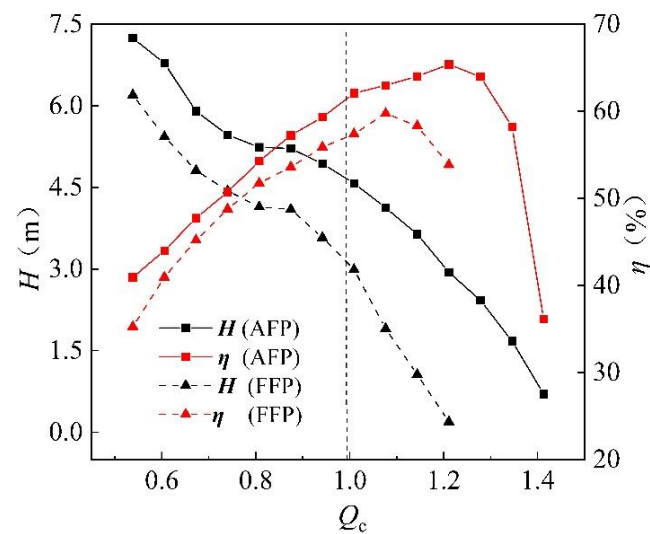


Figure 11. Comparison of head and efficiency of two pumps.

4.2. External Characteristics

The comparison in Figure 11 shows that the steady characteristics of the AFP and FFP have significant differences, so it is assumed that the external characteristics of the two pumps should also be different during shutdown transition. Figure 12a,b show the variations in speed n , flow Q , and torque T with time during shutdown transition for the AFP and FFP. During shutdown transition, the variation pattern of n , Q , and T is the same for the two pumps, where n and Q change from forward to reverse (the Q changes from forward to reverse) and T decreases to 0. The shutdown transition for the two pumps passes through the pumping state, braking state, turbine state, and runaway state. The shutdown transitions of the AFP and FFP took 4.488 s and 6.978 s, respectively. The AFP has a faster shutdown than the FFP. The times that elapsed in the pumping state, braking state, and turbine state for the AFP were 1.638 s, 0.194 s, and 3.156 s, respectively, while the times that elapsed in the above three states for the FFP were 2.178 s, 0.387 s, and 4.913 s, respectively. The three-time nodes for transforming the working states of the AFP were $t_1 = 1.638$ s, $t_2 = 1.832$ s, and $t_3 = 4.988$ s. The three-time nodes for transforming the working states of the FFP were $t_4 = 2.178$ s, $t_5 = 2.565$ s, and $t_6 = 7.478$ s. During the shutdown transition, the deceleration rate of the AFP is 185% and the deceleration rate of the FFP is 180%. The deceleration rate of the AFP is 5% faster than that of the FFP, which means that the AFP stops faster than the FFP. The deceleration rate of the AFP is greater than that of the FFP for n , Q , and T . When $t = 0.5$ s, the pump motor loses power and the dragging torque of the motor becomes 0 N·m. The pump's Q and the impeller's n and T drop rapidly under the action of the water-resistance torque. This state is called the pumping state, which lasts until the Q drops to 0 kg/s, when it ends. The time node $t_1 = 1.638$ s for the shutdown transition of the AFP from the pumping state to the braking state is 0.54 s faster compared to 2.178 s for the FFP. Under the action of the head difference, the n drops further, and the Q changes from forward to reverse; this state is the braking state. The time spent in the braking state is the smallest part of the whole shutdown transition. The time node $t_2 = 1.832$ s for the AFP to switch from the braking state to the turbine state is 0.733 s faster than the time node $t_5 = 2.565$ s for the FFP. Under the action of the head difference, the reverse flow Q further increases, and the reverse speed n of the impeller gradually increases. The rate of the increase in the impeller reverse speed decreases as the torque decreases. Until the torque drops to 0 N·m, the reverse speed n reaches its maximum value. The time when the AFP goes from the turbine state to the runaway state is $t_3 = 4.988$ s, which is 2.49 s faster than the time $t_6 = 7.478$ s for the FFP. When the reverse speed n and backflow Q of the two pumps reach their maximum values, the shutdown transition of each pump unit enters the runaway state. The runaway speeds of the AFP and FFP are approximately 0.84

and 0.80 times the design speed, and the runaway flows are 1.17 and 1.00 times the design flow, respectively. The runaway speed n_r and runaway flow Q_r of the AFP are greater than those of the FFP.

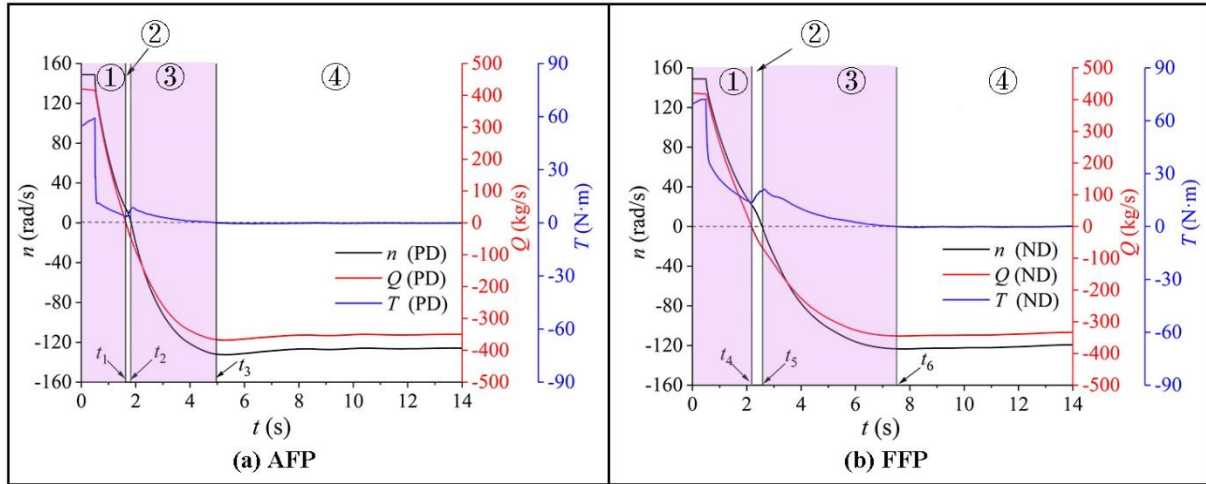


Figure 12. Variations in speed n , flow Q , and torque T over time during shutdown transition. (Regions ①, ②, ③, and ④ represent pumping, braking, turbine, and runaway states, respectively).

Compared with the AFP, there is an SRC in the impeller casing of the FFP, so there is a backflow in the clearance under the effect of the pressure difference. The curves of the axial force F_z and clearance backflow rate Q_t versus time for the FFP were taken out and analyzed, as shown in Figure 13. From Figure 13a, it can be seen that during the shutdown transition of the FFP, the backflow rate Q_t decreases rapidly with time in the pumping state, increases slightly in the braking state, and finally decreases rapidly in the turbine state until it reaches the minimum value of 0.1 kg/s in the runaway state. The trend of change is the same. The F_z decreases sharply in the pumping state, increases slightly in the braking state, and decreases gradually in the turbine state until the axial force stabilizes in the runaway state. The F_z of the AFP during the shutdown transition is significantly lower than that of the FFP. When entering the runaway state, the F_z values of the two pumps are almost equal, and the F_z at this state is about 0.16 times that at the steady state.

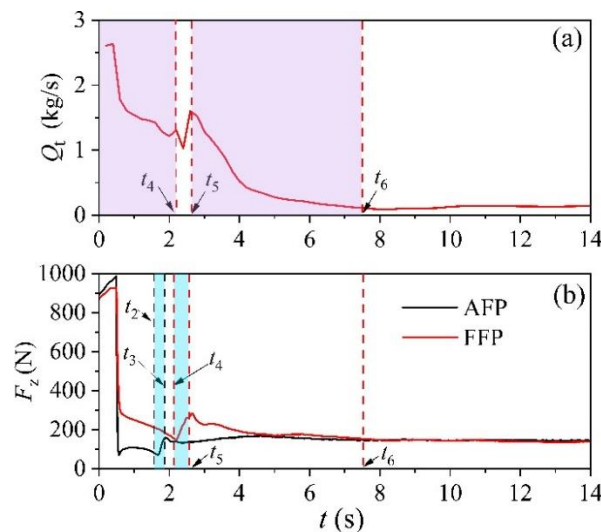


Figure 13. Variation of SRC flow and axial force during shutdown transition. (a) SRC flow. (b) axial force.

Figure 14 shows the variation in the rotor radial force with time during the shutdown transition for the AFP and the FFP. Figure 14a shows the instantaneous radial force F_r and Figure 14b shows the average value of the radial force. From the figure, it can be seen that the two pumps have the same trend of radial force variation during shutdown transition. The F_r gradually decreases in the pumping state and does not change in the braking state. However, the F_r suddenly increases after the unit enters the turbine state until it gradually stabilizes after the unit enters the runaway state. The F_r values of the AFP and FFP reach the maximum values at $t_a = 6.91$ s and $t_f = 5.69$ s, respectively, and the maximum value of the F_r of the AFP is about 1.14 times that of the FFP. In the runaway state, the F_r of the AFP is generally larger than that of the FFP because the AFP's runaway speed is larger than that of the FFP.

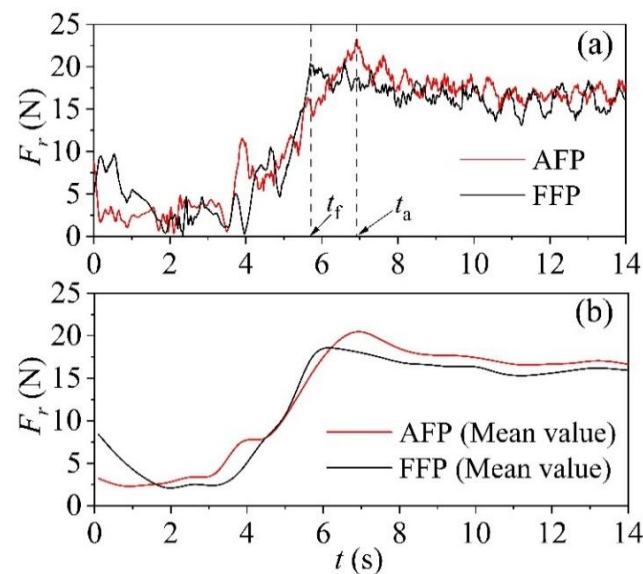


Figure 14. Variation of radial force during shutdown transition. (a) transient data. (b) mean value.

Since the pressure at the impeller outlet is always greater than the impeller inlet during the shutdown transition of the FFP, the clearance backflow always exists, and the backflow rate becomes smaller and smaller with the increase in time. Therefore, to research the influence of the clearance backflow Q_c on the internal flow pattern of the FFP, the pressure distribution and flow line diagram of the impeller at each moment of two pumps were taken out, as shown in Figure 15. The figure shows that in the pumping state, the streamline in the impeller domain of each of the two pumps is relatively smooth. The impeller inlet of the FFP is affected by the Q_c , and a vortex appears near the shroud edge. After entering the braking state, the pressure in the impeller chamber decreases, and the water flows in reverse. Under the influence of the water-resistance torque, the rotational speeds of the impellers of the two pumps gradually decrease, and the flow patterns in the impeller chambers become very turbulent as the speed and flow rate change sharply. There are large areas of backflow and vortex in the impeller I&O. The vortex at the impeller inlet of the FFP gradually shifts to the inlet channel side and the range of the vortex increases. After entering the turbine state, the pressures in the impeller chambers of the two pumps further decrease, the backflow flow of the mainstream increases, and the overall flow patterns become smooth compared with the braking state. In the impeller inlet shroud area of the FFP, there are still vortex, partial-flow, and other undesirable flow patterns. Overall, the flow pattern within the FFP is poorer than that of the AFP. Finally, the water flows of the two pumps are smoother in the runaway state. The impeller has no obvious undesirable flow patterns because the Q_c is low in the runaway state. Overall, the FFP gradually shifts to the IGV side during the shutdown transition. The flow pattern of the impeller chamber of the FFP is worse than that of the AFP because of the impact of the Q_c .

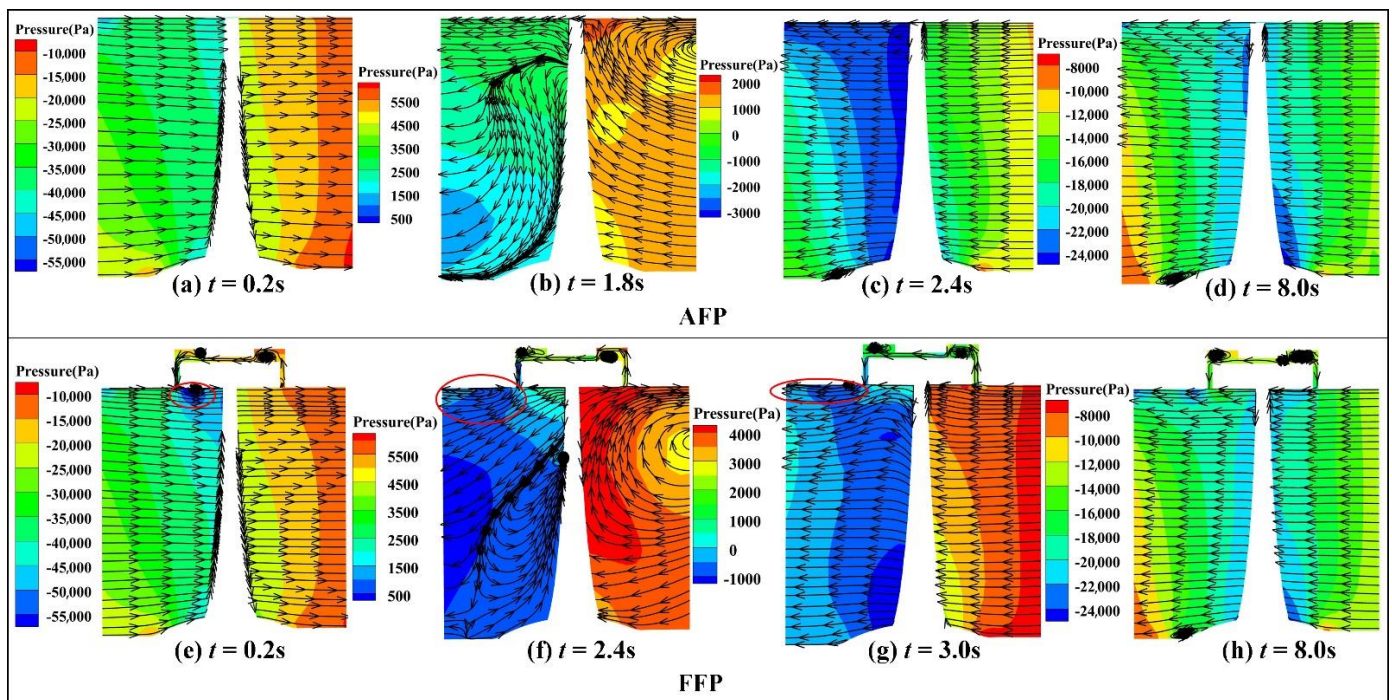


Figure 15. Distribution of pressure and flow lines in impellers of two pumps during shutdown transition.

There is always a clearance backflow in the SRC of the FFP during the shutdown transition. A clearance backflow will cause a local low-pressure area in the impeller inlet near the shroud, resulting in undesirable flow conditions like vortices. Therefore, the clearance backflow will inevitably affect the axial velocity V_a of the impeller I&O of the FFP. Figure 16 shows the parameters of the impeller I&O. The V_a distributions of the AFP and FFP impeller inlet ($\delta d_1 = 0.42$) and outlet ($\delta d_2 = 0.80$) are shown in Figure 17. From Figure 17, it can be found that during the shutdown transition, the V_a values of the impeller I&O of the AFP and the FFP have the same trend; both gradually change from forward to reverse, but the axial velocity values of the two pumps are different under each working condition. In the pumping state, due to the influence of the Q_c , the V_a of the impeller inlet near the shroud of the FFP is significantly lower than that of the AFP in the area of about 18%. The V_a of the impeller outlet near the shroud of the FFP is significantly lower than that of the AFP in the area of about 10%. The effect of the Q_c on the impeller inlet of the FFP is more significant than that on the impeller outlet. At $t = 1.0$ s, the two pumps are still in the pumping state, and the V_a values of the impeller I&O of the FFP are 1.40 and 1.37 times that of the AFP, respectively because the speed of the AFP decreases faster than that of the FFP. When entering the braking state, the V_a of the impeller I&O of the FFP is more significant than that of the AFP in about half of the area near the shroud while the V_a in the other half of the area near the hub is smaller than that of the AFP. In the turbine state, the V_a values at the impeller I&O of the AFP are 1.36 and 1.59 times that of the FFP. In the runaway state, the V_a at the I&O of the FFP is slightly lower than that of the AFP because the n is gradually stabilized, and the Q_r of the AFP is slightly larger than that of the FFP. The deviations in axial velocity in the AFP and FFP in the pumping and turbine states are greater than those in the braking and runaway states. In conclusion, the backflow of the FFP not only affects the flow pattern of the impeller I&O but also affects the axial velocity throughout the shutdown transition.

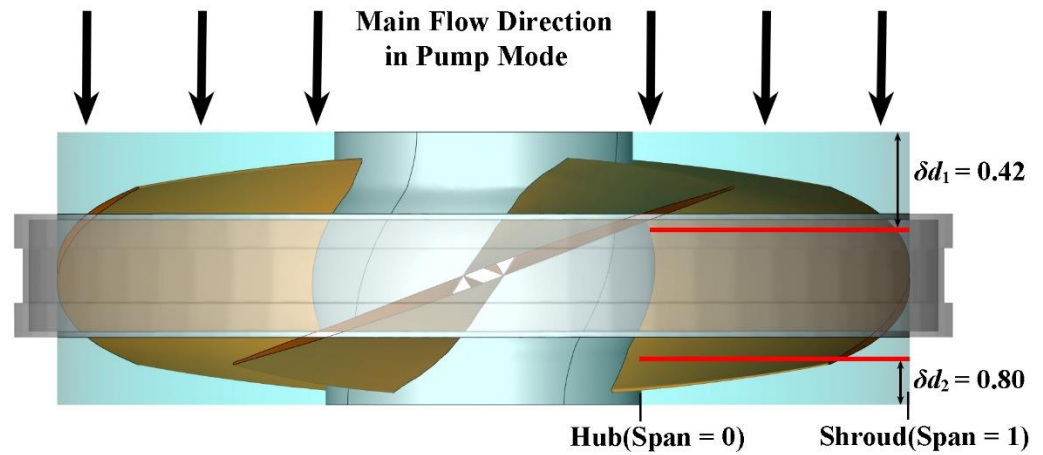


Figure 16. Parameters of the impeller (taking the FFP as an example).

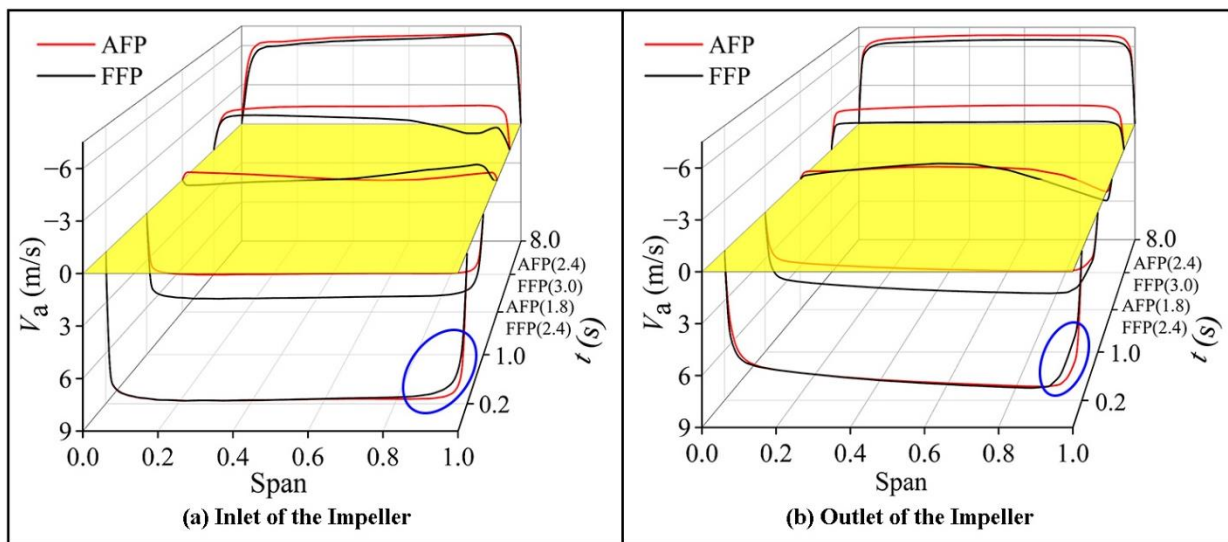


Figure 17. Axial velocity distribution of the two pumps at each moment during the shutdown transition.

4.3. Vortex Identification

From the above analysis, it can be seen that the clearance backflow of the FFP will lead to a backflow vortex in the impeller. However, the specific locations of the vortex at different moments of the shutdown are unknown. Liu et al. [51] proposed the Omega vortex, which has a higher accuracy than the Q-criterion method [52], and its results are a little affected by the threshold value taken. The Omega method accurately identifies the main vortex structural characteristics within the pump in question and can also identify vortices of varying intensities. The Omega vortex identification method decomposes the vortex into rotating and non-rotating parts, as shown in Equation (9).

$$\bar{\omega} = R \times S = V + (R \times S - V) \tag{9}$$

Here, V is the rotating part vortex and $(R \times S - V)$ is the non-rotating part vortex, i.e., pure shear. Since the direction of the rotating part vortex R differs from the total vortex $\bar{\omega}$, the parameter Ω is introduced to represent the ratio of R to $\bar{\omega}$. The expression of Ω is shown in Equation (10). In the application, to prevent Ω from being infinite when the denominator is

0, a smaller positive number ε needs to be added to the denominator, and Equation (10) becomes Equation (11).

$$\Omega = \frac{\|B\|_F^2}{\|A\|_F^2 + \|B\|_F^2} \tag{10}$$

$$\Omega = \frac{\|B\|_F^2}{\|A\|_F^2 + \|B\|_F^2 + \varepsilon} \tag{11}$$

Here, A is the symmetry tensor and B is the anti-symmetry tensor. It can be found that Ω is taken in the range of $0 \leq \Omega \leq 1$. When $\Omega = 0$, the flow field is spinless, $\Omega = 1$ means that the flow field performs a rigid body rotation, and $\Omega > 0.5$ means the symmetry tensor A is smaller than the anti-symmetry tensor B . In this paper, we use $\Omega = 0.52$ to determine the presence of vortices in the flow field, and the value of ε is based on the approximate formula $\varepsilon = 0.002Q_{\max}$ proposed by Dong et al. [53]. A 3D schematic of the impeller domain was taken out to facilitate the analysis of the vortex in the impeller, as shown in Figure 18. Figure 19 shows the Omega vortex distribution within the impeller during the shutdown transition for both the AFP and FFP. As the AFP has selected the SRC as 0.15 mm, the clearance leakage is small at this clearance value; only at the leading edge (LE) of the suction side (SS) of the blade, a smaller clearance leakage vortex [54] appears, as shown in Figure 19a. Under the pumping state, the pressure difference between the I&O of the impeller of the FFP is significant, resulting in a significant backflow in the SRC, thus forming a clearance backflow vortex at the junction of the clearance outlet and the SS of the blade. The number of clearance backflow vortices equals the number of blades and is symmetrically distributed, as shown in Figure 19f. Under the braking and turbine states, the main flow in the AFP starts to reverse. Due to the water resistance, the speed of the impeller gradually drops to 0 and starts to rotate in reverse, with a smaller clearance leakage vortex appearing at the trailing edge (TE) of the SS of the AFP. Under the braking state, due to the reduction in the I&O pressure difference, the clearance backflow of the FFP decreases, and the size of the vortex also decreases significantly. There are four symmetrically distributed filamentous vortices at the clearance corners. The main water flow collides with the blade in the backward flow to produce flow separation, and the separation vortex is formed at the TE of the SS of the blade. As the FFP enters the turbine state, the backflow rate increases, the flow separation at the TE of the SS of the blade intensifies, and the size of the separation vortex becomes larger. Due to the reduction in the clearance backflow, the size of the filamentary vortex at the clearance corners has also been reduced. Finally, under the turbine state, the AFP does not exist in the apparent vortex, while the FFP clearance I&O and blade junction are large clearance backflow vortices. There are also vortices at the LE of the SS of the blades near the hub area. In general, during the shutdown transition, the vortex inside the impeller of the FFP is larger and mainly exists at the junction of the SRC inlet and outlet and blade and the LE of the SS, while the vortex inside the AFP is smaller.

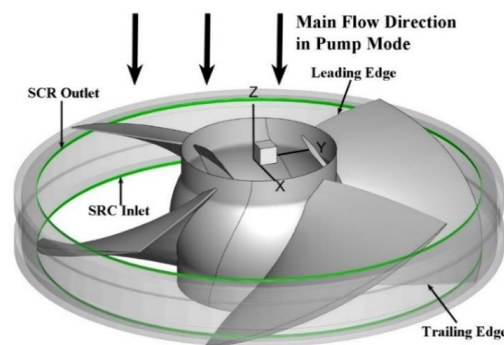


Figure 18. Schematic diagram, in 3D, of each parameter in the impeller domain (taking the FFP as an example).

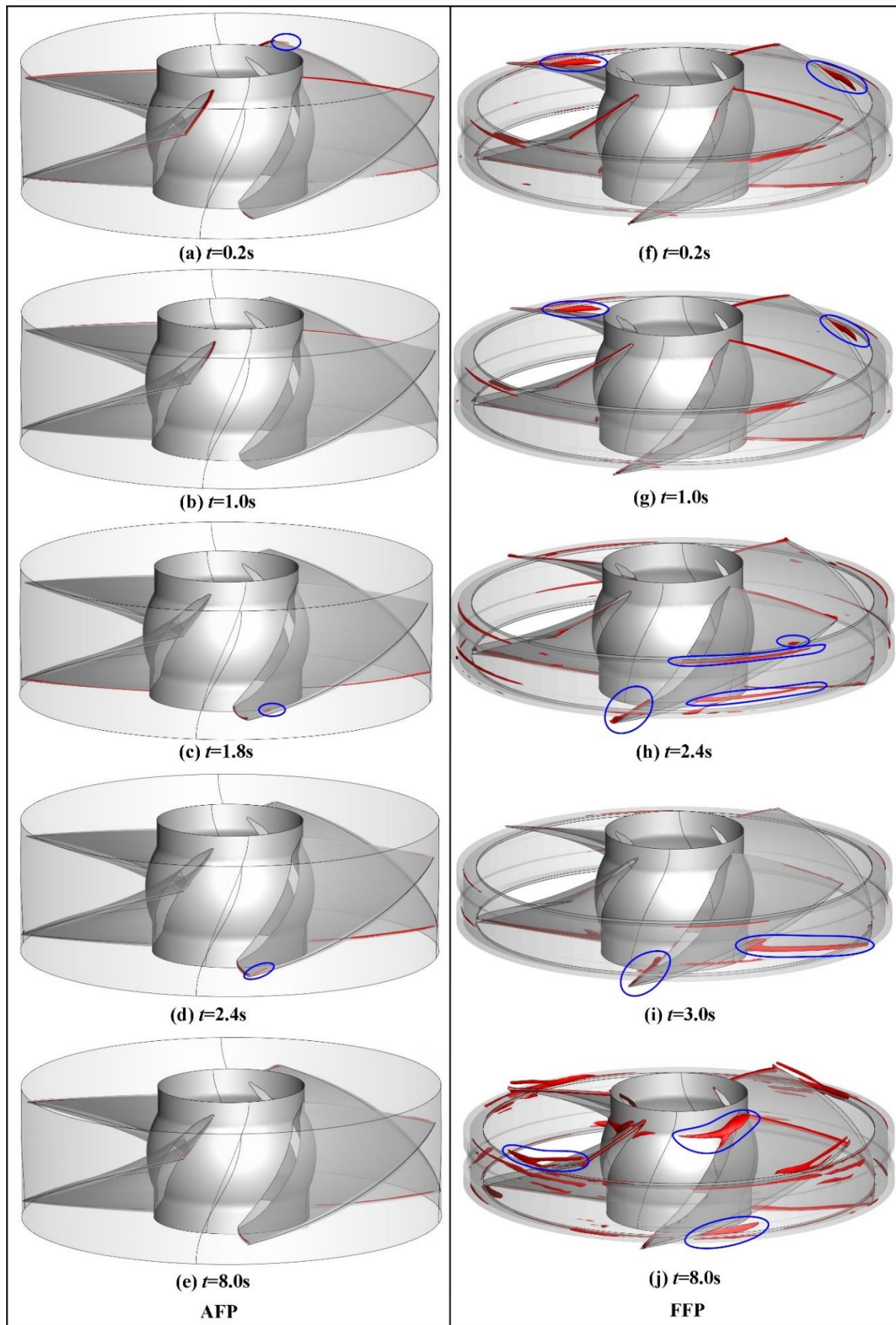


Figure 19. The vortex distribution of the impellers of the two pumps at each moment during the shutdown transition.

4.4. Entropy Production

Since there is a correlation between the distribution of EP and the evolution of vortices, and there are always clearance backflow vortices and flow separation in the impeller during the shutdown transition of the FFP, it is necessary to study the EP. During the operation of the pump, there is a continuous loss of mechanical energy so that the entropy gain in the system is always greater than zero. The primary sources of EP in the device are undesirable flow regimes and energy conversions. Because of water’s high specific heat capacity, energy conversion is not considered when calculating the entropy yield. The total EP S in the pump consists of three main components, direct dissipative EP S_z , turbulent dissipative EP S_t , and wall EP S_b [55,56], as shown in Equation (12).

$$S = S_z + S_t + S_b \tag{12}$$

$$S_z = \int_V \dot{S}_z^* dV \tag{13}$$

$$S_t = \int_V \dot{S}_t^* dV \tag{14}$$

$$S_b = \int_A \dot{S}_b^* dA \tag{15}$$

Here, \dot{S}_z^* , \dot{S}_t^* , and \dot{S}_b^* are the three types of EPR.

$$\dot{S}_z^* = \frac{\mu}{T} \left[\left(\frac{\partial \bar{u}}{\partial y} + \frac{\partial \bar{v}}{\partial x} \right)^2 + \left(\frac{\partial \bar{u}}{\partial z} + \frac{\partial \bar{w}}{\partial x} \right)^2 + \left(\frac{\partial \bar{v}}{\partial z} + \frac{\partial \bar{w}}{\partial y} \right)^2 \right] + 2 \frac{\mu}{T} \left[\left(\frac{\partial \bar{u}}{\partial x} \right)^2 + \left(\frac{\partial \bar{v}}{\partial y} \right)^2 + \left(\frac{\partial \bar{w}}{\partial z} \right)^2 \right] \tag{16}$$

Here, \bar{u} , \bar{v} , and \bar{w} are the average velocity components; T is the temperature.

The turbulent dissipative EPR is

$$\dot{S}_t^* = \frac{\mu + \mu_t}{T} \left[\left(\frac{\partial u'}{\partial y} + \frac{\partial v'}{\partial x} \right)^2 + \left(\frac{\partial u'}{\partial z} + \frac{\partial w'}{\partial x} \right)^2 + \left(\frac{\partial v'}{\partial z} + \frac{\partial w'}{\partial y} \right)^2 \right] + 2 \frac{\mu + \mu_t}{T} \left[\left(\frac{\partial u'}{\partial x} \right)^2 + \left(\frac{\partial v'}{\partial y} \right)^2 + \left(\frac{\partial w'}{\partial z} \right)^2 \right] \tag{17}$$

where μ_t is the turbulent dynamic viscosity and u' , v' , and w' are the pulsation velocity components.

For the SST $k - \omega$ turbulence model, \dot{S}_t^* can be calculated using the approximate Equation (18):

$$\dot{S}_t^* = \beta \cdot \frac{\rho f k}{T} \tag{18}$$

Here, k is the turbulent energy, $\beta = 0.09$, and f is the frequency.

The formula for calculating the wall EPR has been given by Zhang et al. [57], as shown in Equation (19).

$$\dot{S}_b^* = \frac{\tau_w \cdot u_p}{T} \tag{19}$$

Here, u_p is the average velocity vector.

EPR calculations were performed for two pump trains to investigate the difference in the location of energy loss during shutdown transition for the two pumps. Figure 20 shows the EPR in the two pumps over time, with P_L as the EP. Figure 21 shows the parameters for each section. Figure 22 shows a 3D schematic of the 0.95 blade height. Figure 23 shows the distribution of EPR in each section of the pump. Figure 24 is a 3D schematic of a blade height span of 0.95.

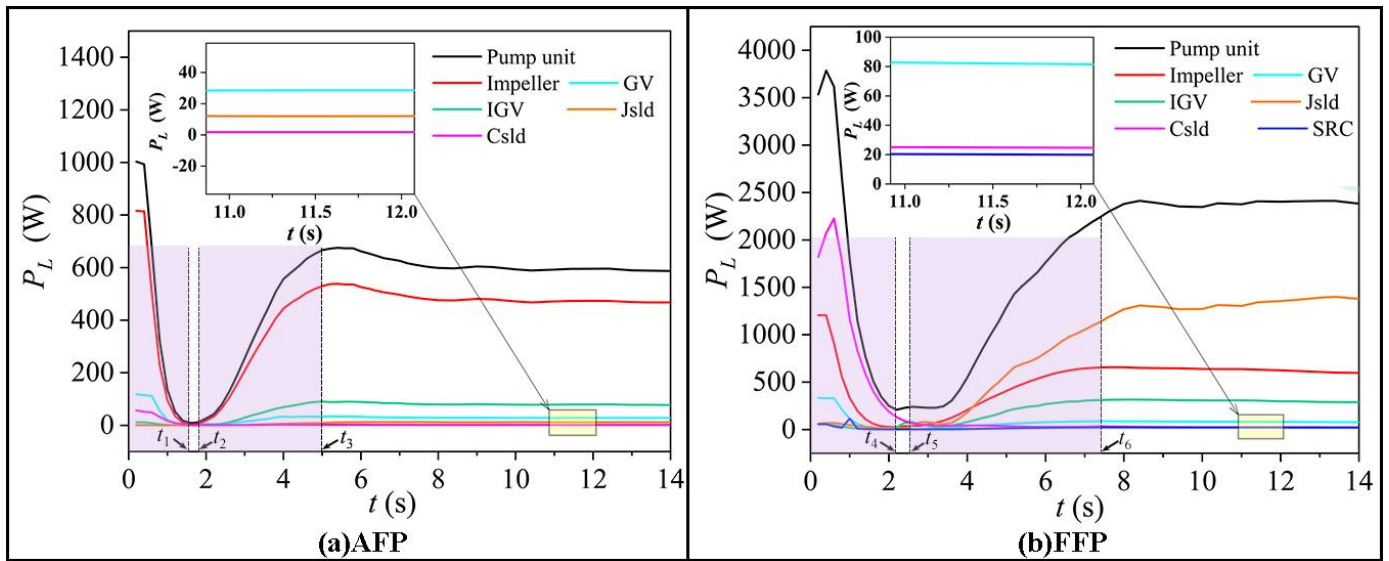


Figure 20. The EPR in the two pumps over time during shutdown transition.

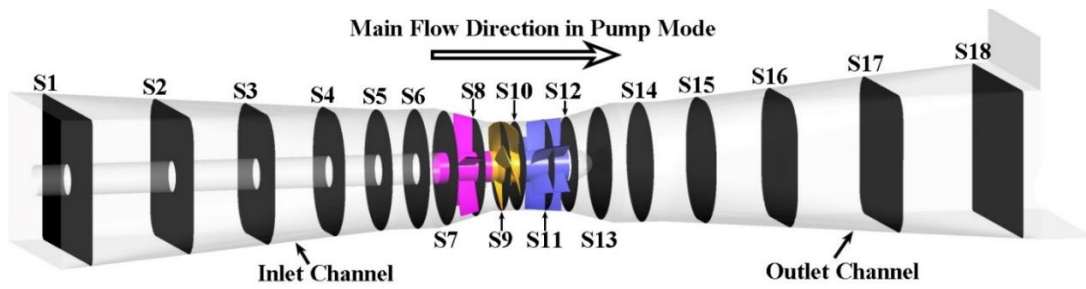


Figure 21. Schematic diagram, in 3D, of each cross-section within the pump unit.

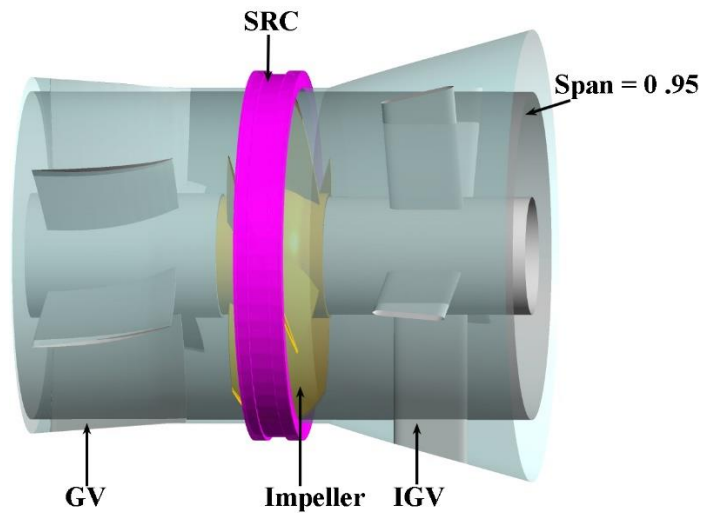


Figure 22. Schematic, in 3D, of a blade height span of 0.95.

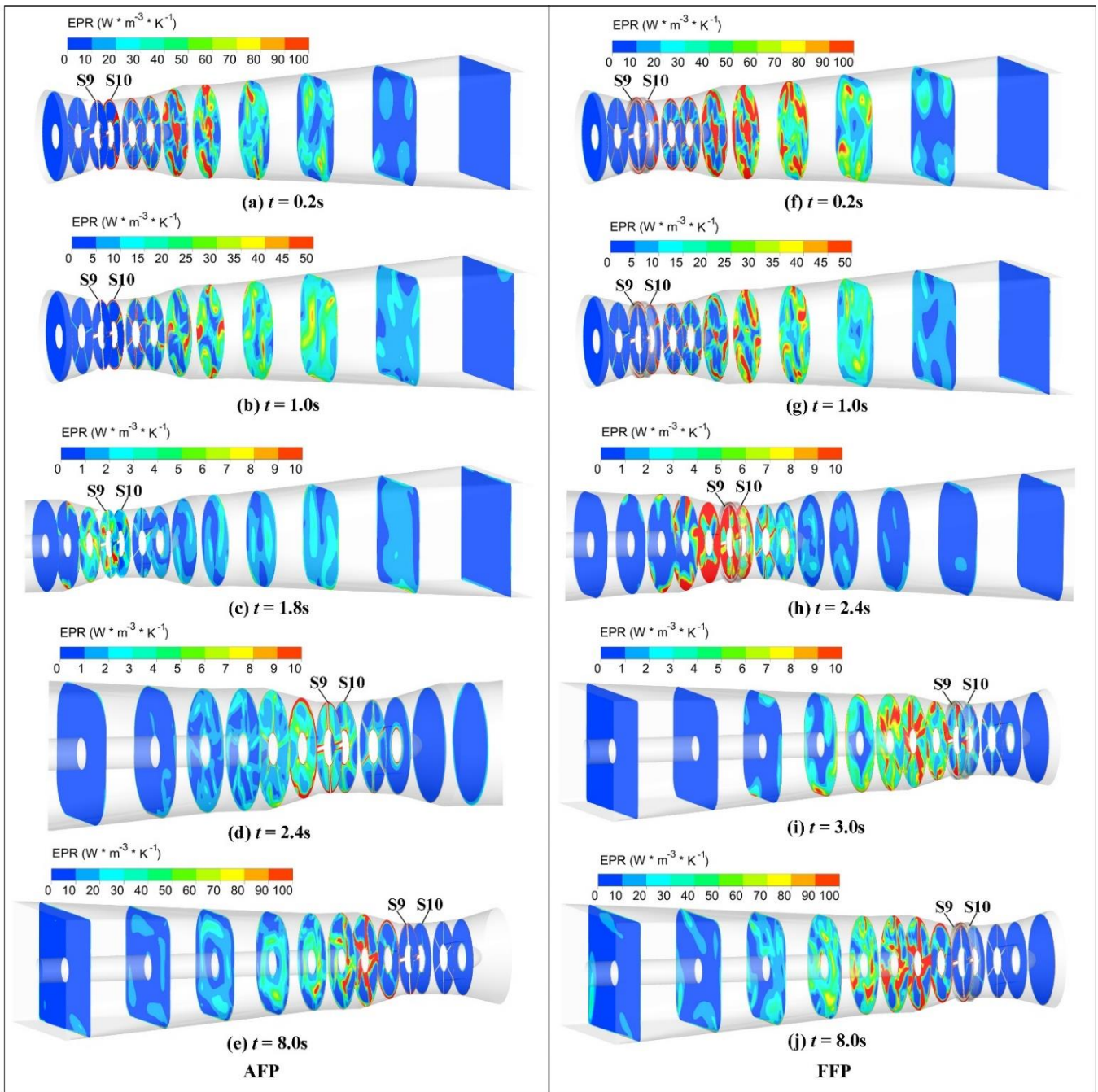


Figure 23. Distribution of the EPR at each section of the two pumps during the shutdown transition.

Figures 20 and 23 show that during the shutdown transition, the internal EP of the AFP and the FFP follow the same trend with time, with both decreasing and then increasing with time and finally remaining stable in the runaway state. The hydraulic losses in the two pumps are mainly concentrated in the impeller and its downstream area under the pumping state. The internal EP of the AFP unit is mainly concentrated in the impeller and GV. In contrast, the internal EPR of the FFP is mainly concentrated in the outlet channel, impeller, and GV. This is due to the dramatic reduction in the impeller’s ability to work when the motor is disconnected, resulting in a dramatic reduction in flow and rotational speed. After the water has passed through the impeller, undesirable flow patterns such as vortices, backflows, and flow separation occur. The large velocity gradients lead to significant hydraulic losses in the impeller.

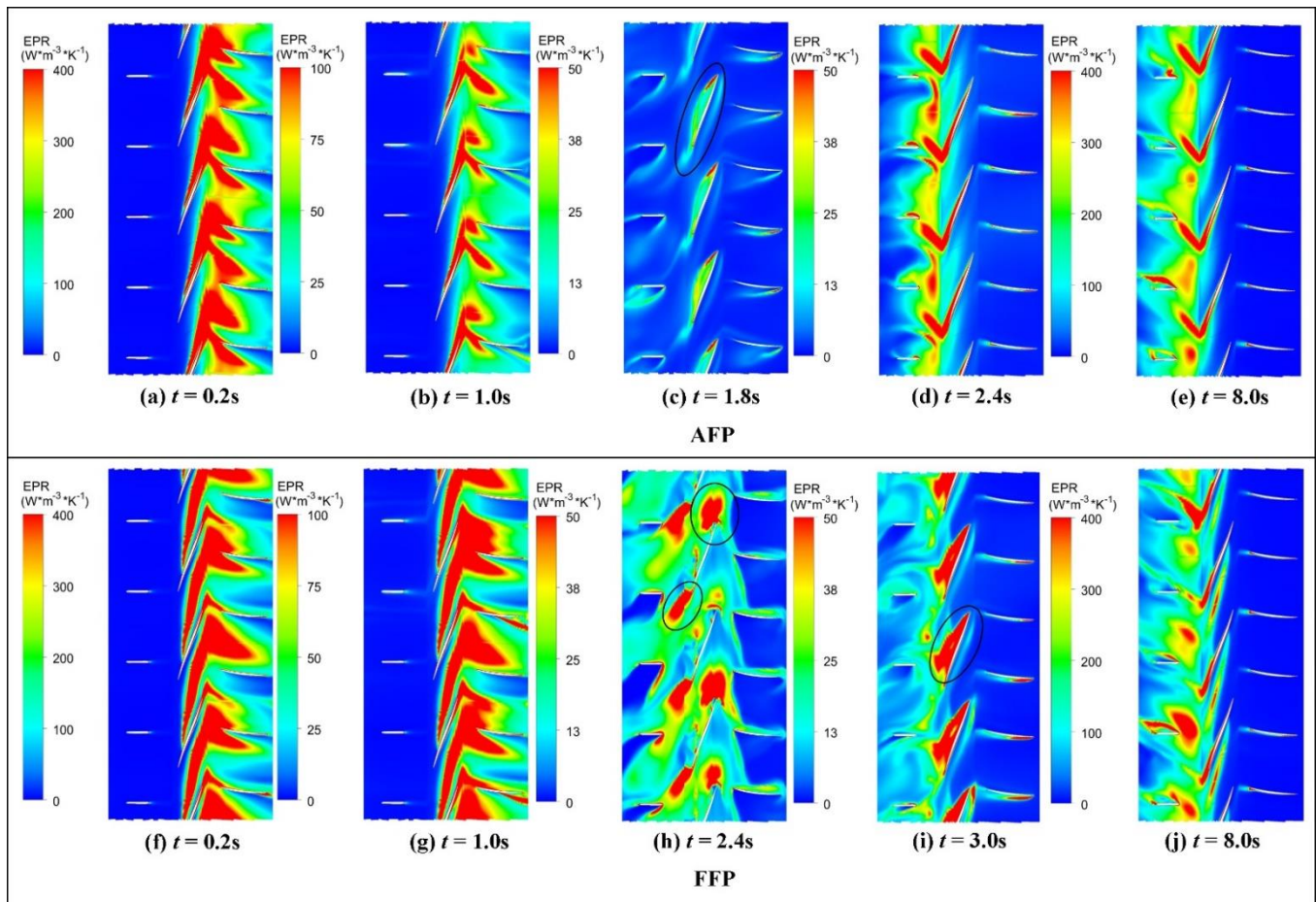


Figure 24. The EPR distribution of the pump sections of the two pumps.

Due to the clearance backflow, the impeller I&O of the FFP produce a clearance leakage vortex in the near-wall area. Consequently, the velocity distribution is more uneven, resulting in more significant hydraulic losses than in the AFP. Under the pumping state, the hydraulic losses decrease rapidly as the rotational speed approaches zero. As can be seen from Figure 23a,f, the distribution of high EPR within the two pumps is essentially the same at the pumping state, but the range of high EPR within the FFP is broader than that of the AFP, confirming the results in Figure 23. Figure 23b,g shows the high EPR distribution clouds for each section of the two pumps at $t = 1$ s. At this point, the motor is disconnected for 0.5 s. Because of the dramatic reduction in rotational speed, its internal high EPR is reduced compared to that at $t = 0.2$ s. However, the internal high-EPR range of the FFP is still broader than that of the AFP.

When the two pumps enter the braking state, the main flow at the impeller inlet is reduced. At this stage, the hydraulic losses within the AFP and FFP units are the lowest during the shutdown transition, as the hedging between the forward and reverse flow is reduced. However, as shown in Figure 23c,h, the area of EPR within the two pumps shifts towards the inlet channel side as the flow reverses. The passage between the impeller and IGV of the FFP is filled with areas of high EPR. At the same time, the AFP has a minor region of high EPR in the near-wall area of the impeller and IGV, indicating that the hydraulic losses within the FFP are greater than those of the AFP at this moment.

When the two pumps enter the turbine state, the main flow is violently pushed against the impeller by the effect of the upstream and downstream heads and the impeller's reverse speed and flow rate increase rapidly. As shown in Figure 23d,i, the high-EPR region in both pumps is concentrated on the impeller's and GV's surfaces. This is because of the flow separation on the surface of the impeller as the water flows violently against the blades.

The energy conversion between high- and low-velocity water bodies is strong, and the hydraulic loss increases rapidly. Under the turbine state, the clearance backflow of the FFP causes leakage vortices in the impeller I&O, so the total hydraulic loss is greater than the AFP; the hydraulic losses of the AFP are mainly concentrated in the impeller and IG. In contrast, the hydraulic losses of the FFP unit are mainly concentrated in the inlet channel, impeller, and IG.

As the torque gradually approaches 0, the two pumps enter the runaway state. At this point, the reverse speed and flow rate reach their maximum values and gradually stabilize and the hydraulic losses ΔH in two pumps also stabilize. As the runaway speed is lower than the initial speed in the steady state, ΔH in the two pumps in the runaway state is also lower than in the steady state. Figure 19 shows a significant flow separation at the TE of the impeller of the FFP under the runaway state. The clearance backflow will also produce leakage vortices at the impeller I&O, resulting in poor flow patterns and large velocity gradients in the impeller and inlet channels. The total hydraulic loss of the FFP is approximately 4.06 times that of the AFP. As shown in Figure 23e,j, the high EPR in both pumps is mainly concentrated in the inlet channel, IG, and impeller. The distribution of high EPR within IGs is consistent with the number of IG blades due to the large angle of attack of the water flow with the IG after exiting the impeller. As a result, significant flow separation occurs at the surface of the IG.

As the hydraulic losses within the AFP and the FFP are mainly concentrated in the impeller, GV, and IG, the cross-sectional expansion of the pump section at span = 0.95 was taken out for analysis, as shown in Figure 24. Overall, with the development of the shutdown transition, the high-EPR area within the two pump units gradually shifted toward the IG, with the high-EPR area first decreasing and then increasing, and the range of high EPR within the pump section of the FFP was greater than that of the AFP. From Figure 24a,f, it can be seen that under pumping state, the high-EPR area of the two pumps is mainly concentrated in the SS of the impeller and the non-leaf area between the impeller and the GV, which is due to the dynamic and static interference between the impeller and the GV, making the pressure gradient larger. The range of high EPR at the SS of the blades is greater in the FFP than in the AFP due to the effect of clearance backflow. Figure 24b,g show the pumping state when the unit is stopped for 0.5 s. The distribution of high EPR in the impeller and GV regions is consistent with the steady state, but the range is significantly reduced due to the significant speed reduction. As the speed drop rate of the FFP is lower than that of the AFP in the pump state, the value of the velocity gradient within the FFP is larger than that of the AFP, and the range of high EPR is also larger than that of the AFP. Figure 24c,h shows the pump entering the braking state, at which point the flow has started to back up. There is significant flow separation between the two pumps at the impeller, GV, and IG surfaces, but due to the lower flow rate at this point, the range of high EPR is much reduced compared to the pumping state.

As shown in Figure 24, the FFP has localized areas of high EPR at both the head and tail of the impeller due to the presence of clearance vortices in the impeller chamber. In contrast, the AFP has a small region of high EPR at the SS of the impeller and the end of the GV. Therefore, the area of high EPR in the FFP under the braking state is larger than in the AFP. Figure 24d,i show the pump unit entering the turbine state. As the backflow rate increases, the velocity gradient in the two pumps increases, and the range of high EPR is greater than in the braking state. As the flow separation occurs at the SS of the impeller of the FFP, almost 3/4 of the length of the blade surface is the high-EPR area. The high-EPR area in AFP is concentrated in the SS of the impeller and the dynamic and static interference zone between the impeller and the GV. Overall, the high-EPR region in the FFP is larger than that in the AFP under the turbine state when two pumps enter the runaway state, as shown in Figure 24e,j. As the backflow rate continues to increase, the flow separation between the SS of the impeller and the head of the IG of the two pumps increases. The flow separation point is shifted from the tail of the impeller to the middle and the high-EPR range is further increased. The velocity gradient of the FFP is

also greater due to the presence of more clearance backflow vortices and flow separation vortices. The range of high EPR for the FFP is wider than for the AFP. The conclusions of Figure 24 remain consistent with Figure 20, indicating that the EP theory and results are accurate and credible.

5. Conclusions

This study compared the shutdown transition of the axial-flow pump with that of the full-flow pump. The external characteristics, runaway characteristics, and pressure pulsation characteristics of the FFP were investigated using model tests. Transient numerical simulations of the shutdown transition of the two pumps were carried out. First, the differences in external and internal characteristics between the two pumps were investigated. A comparison of the external characteristics, runaway, and pressure pulsation data showed that the numerical calculations were accurate. The reasons for differences in the shutdown characteristics of the two pumps were investigated from the aspects of the internal flow field, vortex, and EP. The conclusions were as below:

- (1) Same rules for the AFP and FFP: During the shutdown transition, the two pumps experience a pumping state, braking state, turbine state, and runaway state, with the braking state being of the smallest proportion; each external characteristic of the AFP and FFP (speed, flow, torque, and axial and radial forces) follows the same trend; the rotational speed and flow rate of the two pumps gradually change from forward to reverse; the rotor radial force first decreases and then increases until it enters the turbine state and gradually stabilizes; the axial force decreases continuously, increases only slightly in the braking state, and finally stabilizes in the runaway state; the high-EPR area within the two pumps gradually shifts toward the IGV, and the high-EPR area first decreases and then increases; the hydraulic losses of the AFP and FFP units under the braking state are the lowest. Both pumps' high-EPR regions are mainly concentrated in the inlet channels, IGVs, and impellers.
- (2) Different rules for the AFP and FFP: During the shutdown transition, the rates of decrease in torque, speed, and flow of the AFP are faster than those of the FFP, which means that the AFP is faster than the FFP. Due to the clearance backflow, the impeller of the FFP generates clearance backflow vortices near the I&O, and the overall flow pattern in the impeller is worse than that of the AFP, resulting in a greater hydraulic loss than that in the AFP. Under the runaway state, the hydraulic loss of the FFP is approximately 4.06 times that of the AFP. The AFP's runaway speed and flow rate are greater than the FFP's. During the shutdown transition, the axial force of the AFP is significantly lower than that of the FFP. The maximum rotor radial force of the AFP is approximately 1.14 times that of the FFP. In the pumping state, due to the effect of clearance backflow, the axial velocity of about 10% of the impeller inlet area near the FFP shroud is significantly lower than that of the AFP. In the turbine state, the axial velocity values at the impeller inlet and outlet of the AFP are 1.36 and 1.59 times higher than those of the FFP, respectively.

During the shutdown transition, the vortex inside the impeller of the FFP is larger. It is mainly located in the corner of the SRC, at the junction of the clearance inlet and outlet and the main flow, as well as the LE of the SS of the impeller, while the AFP has only a small amount of leakage vortices at the SS of the impeller. There are more vortices inside the FFP impeller, mainly clearance backflow vortices and flow separation vortices, and they are mainly distributed in the corners of the SRC, at the junction of the I&O of the clearance and the main flow and the LE of the SS of the impeller. The EP of the AFP unit is mainly concentrated in the impeller and GV, whereas the EP of the FFP unit is mainly concentrated in the outlet channel, impeller, and GV. Under the runaway state, there is a noticeable flow separation at the TE of the impeller of the FFP. At the same time, there is also a leakage vortex at the I&O of the impeller, resulting in a poor flow pattern and a large velocity gradient in the impeller and inlet channel. Due to the effect of the clearance backflow, the area of high EPR at the SS of the impeller of the FFP is larger than that of the AFP.

Author Contributions: H.J.: data curation, methodology, software, writing, experiment. J.S.: resources, financial support. G.Y.: writing—review and editing. M.W.: review, editing. S.C.: theoretical guidance, financial support. All authors have read and agreed to the published version of the manuscript.

Funding: This work was supported by the National Natural Science Foundation of China (51076136), National Science and Technology Planning Project (2006BAB04A03), Natural Science Foundation of Jiangsu Province (BK2008217), Water Conservancy Science and Technology Project of Jiangsu Province (Grant no. 2009053), and Priority Academic Program Development of Jiangsu Higher Education Institutions (Grant number PAPD).

Institutional Review Board Statement: Not applicable.

Informed Consent Statement: Not applicable.

Data Availability Statement: Data available on request due to restrictions eg privacy or ethical. The data presented in this study are available on request from the corresponding author. The data are not publicly available due to the unfinished project involving these data.

Conflicts of Interest: The authors declare no conflict of interest.

Nomenclature

A : The symmetry tensor

B : The anti-symmetry tensor

C_p : Pressure pulsation coefficient

d_1 : The tip clearance of the AFP, mm

d_2 : The stator and rotor clearance of the FFP, mm

dt : Single time step

D_1 : The radii of the impeller hub, mm

D_2 : The radii of the impeller shroud, mm

f : Frequency, Hz

F_z : Axial force, N

F_r : Radial force, N

H : Head, m

H_c : Head coefficient

H_d : Design head, m

J_G : The rotational inertia of the rotating parts of the pump unit, kg/m^2

k : The turbulent energy, m^2/s^2

n : Impeller revolution, rpm

n_r : Speed of rotation of the runaway, rpm

N_f : Number of steps in one revolution of the impeller

p : Pressure, Pa

P : Instantaneous pressure, Pa

P_L : Energy loss, W

Q : Mass Flow rate, kg/s

Q_c : Flow coefficient

Q_d : Design flow, kg/s

Q_r : Runaway flow, kg/s

Q_t : SRC backflow, kg/s

R : The rotating part vortex

$(R \times S - V)$: The non-rotating part vortex

S_z : The direct dissipative entropy production, $\text{W} * \text{K}^{-1}$

S_t : The turbulent dissipative entropy production, $\text{W} * \text{K}^{-1}$

S_b : The wall entropy production, $\text{W} * \text{K}^{-1}$

S : The total entropy production, $\text{W} * \text{K}^{-1}$

S_z^* : The direct dissipative entropy production rate, $\text{W} * \text{m}^{-3} * \text{K}^{-1}$

S_t^* : The turbulent dissipative entropy production rate, $\text{W} * \text{m}^{-3} * \text{K}^{-1}$

S_b^* : The wall entropy production rate, $\text{W} * \text{m}^{-3} * \text{K}^{-1}$

t : The time, s
 t_a, t_f : The time when the radial force of the AFP and FFP reaches the maximum value, s
 T : The temperature, K
 T_D : The dragging torque of the motor, N·m
 T_F : The loss torque of the motor fan, N·m
 T_I : The torque of inertia, N·m
 T_O : The oil viscous resistance torque of the thrust head and slip rotor, N·m
 T_R : The frictional torque of the radial bearing, N·m
 T_W : The water torque of the pump, N·m
 T_Z : The frictional torque of the thrust bearing, N·m
 u : Circumferential velocity, m/s
 u_p : The average velocity vector at the center of the first grid layer in the near-wall zone, m/s
 V_a : Axial velocity, m/s
 V : The rotating part vortex
 Greek letters and mathematical operators
 β : Empirical coefficient
 η : Efficiency, %
 μ_t : The turbulent dynamic viscosity, Pa·s
 ρ : Liquid density, kg/m³
 ω : The instantaneous angular speed of the impeller, rad/s
 Ω : The ratio of R to ω
 ΔC_p : The maximum difference of the pressure pulsation coefficient
 Δh : Head difference, Pa
 \bar{P} : Average pressure, Pa
 Δn_r : The maximum difference of the runaway speed, rpm
 $\bar{u}, \bar{v},$ and \bar{w} : The components of the mean velocity in the $x, y,$ and z directions, m/s
 $u', v',$ and w' : The pulsation velocity components in the $x, y,$ and z directions, m/s
 ω : Total vortex
 Abbreviations
 2D: Two-dimensional
 3D: Three-dimensional
 AFP: Axial-flow pump
 BPF: Blade passing frequency
 CFD: Computational fluid dynamics
 EP: Entropy production
 EPR: Entropy production rate
 FFP: Full-flow pump
 GV: Guide vane
 IGV: Inlet guide vane
 I&O: Inlet and outlet
 LE: Leading edge
 PP: Pressure pulsation
 PS: Pressure side
 SRC: Stator rotor clearance
 SS: Suction side
 SUT: Start-up transition
 TE: Trailing edge
 UDF: User-Defined Function

References

1. Tang, F.; Liu, C.; Zhou, J.; Yuan, J.; Cheng, L.; Yan, B.; Xie, W. "S" shaped hydrofoil bi-directional axial-flow pump design. *Pump Technol.* **2002**, *5*, 11–13.
2. Liu, H.; Guo, Q.; Shi, L.; Tang, F.; Dai, L.; Shen, J.; Liu, J. Lift-drag characteristics of S-shaped hydrofoil under different cloud cavitation conditions. *Ocean Eng.* **2023**, *278*, 114374. [[CrossRef](#)]
3. Liu, Y.; Zhe, H.; Xue, Y.; Tan, J.; Yuan, P.; Zhang, Q. Effects of vortex generator on the hydrodynamic characteristics of hydrofoil and horizontal axis tidal turbine. *Phys. Fluids* **2023**, *35*, 035104. [[CrossRef](#)]
4. Zang, W.; Zhang, Y.; Zheng, Y.; Zhang, J.; Guan, D.W.; Fernandez-Rodriguez, E. On the impact of waves and turbulence on the power fluctuations and wake structure of a tidal-stream turbine. *Phys. Fluids* **2023**, *35*, 055115.

5. Derakhshan, S.; Ashoori, M.; Salemi, A. Experimental and numerical study of a vertical axis tidal turbine performance. *Ocean Eng.* **2017**, *137*, 59–67. [[CrossRef](#)]
6. Abonai, C.; Xi, J. Operation and management experience of Lance tidal power plant in France. *Express Water Resour. Hydropower Inf.* **2011**, *32*, 29–32. (In Chinese) [[CrossRef](#)]
7. Wang, Z.; Yang, X.; Xiao, Y. Hydraulic performance optimization of bidirectional tidal power turbine. *J. Drain. Irrig. Mach. Eng.* **2010**, *28*, 417–421. (In Chinese)
8. Meng, F.; Li, Y.; Pei, J. Energy Characteristics of Full Tubular Pump Device with Different Backflow Clearances Based on Entropy Production. *Appl. Sci.* **2021**, *11*, 3376. [[CrossRef](#)]
9. Shi, L.; Yuan, Y.; Jiao, H.; Tang, F.; Cheng, L.; Yang, F.; Jin, Y.; Zhu, J. Numerical investigation and experiment on pressure pulsation characteristics in a full tubular pump. *Renew. Energy* **2021**, *163*, 987–1000. [[CrossRef](#)]
10. Shi, L.; Zhang, W.; Jiao, H.; Tang, F.; Wang, L.; Sun, D.; Shi, W. Numerical simulation and experimental study on the comparison of the hydraulic characteristics of an axial-flow pump and a full tubular pump. *Renew. Energy* **2020**, *153*, 1455–1464. [[CrossRef](#)]
11. Shi, L.; Zhu, J.; Yuan, Y.; Tang, F.; Huang, P.; Zhang, W.; Liu, H.; Zhang, X. Numerical Simulation and Experiment of the Effects of Blade Angle Deviation on the Hydraulic Characteristics and Pressure Pulsation of an Axial-Flow Pump. *Shock. Vib.* **2021**, *2021*, 6673002. [[CrossRef](#)]
12. Liu, J.; Li, Z.; Wang, L.; Jiao, L. Numerical Simulation of the Transient Flow in a Radial Flow Pump during Stopping Period. *J. Fluids Eng.* **2011**, *133*, 111101. [[CrossRef](#)]
13. Wu, D.; Wu, P.; Yang, S.; Wang, L. Transient Characteristics of a Closed-Loop Pipe System During Pump Stopping Periods. *J. Press. Vessel Technol.* **2014**, *136*, 021301. [[CrossRef](#)]
14. Zhang, X.; Hu, C.; Tang, F.; Yang, F.; Song, X.; Liu, C.; Shi, L. Numerical and Experimental Study on the Shutdown Transition Process of a Large Axial Flow Pump System Focusing on the Influence of Gate Control. *J. Mar. Sci. Eng.* **2023**, *11*, 280. [[CrossRef](#)]
15. Liu, Y.; Zhou, J.; Zhou, D. Transient flow analysis in axial-flow pump system during stoppage. *Adv. Mech. Eng.* **2017**, *9*, 1687814017723280. [[CrossRef](#)]
16. Su, W.; Li, X.; Xia, Y.; Liu, Q.; Binama, M.; Zhang, Y. Pressure fluctuation characteristics of a model pump-turbine during runaway transient. *Renew. Energy* **2021**, *163*, 517–529. [[CrossRef](#)]
17. Trivedi, C.; Cervantes, M.; Gandhi, B.; Ole, F.D. Experimental investigations of transient pressure variations in a high head model Francis turbine during start-up and shutdown. *J. Hydrodyn.* **2014**, *26*, 277–290. [[CrossRef](#)]
18. Deng, Y.; Xu, J.; Li, Y.; Zhang, Y.; Kuang, C. Research on Energy Loss Characteristics of Pump-Turbine during Abnormal Shutdown. *Processes* **2022**, *10*, 1628. [[CrossRef](#)]
19. Zhang, Y.; Ji, Y.; Zhao, Y. Deep analysis of the transient behavior of centrifugal pumps during startup and shutdown. *Meas. Control.* **2022**, *55*, 155–163. [[CrossRef](#)]
20. Feng, J.; Ge, Z.; Zhang, Y.; Zhu, G.; Wu, G.; Lu, J.; Luo, X. Numerical investigation on characteristics of transient process in centrifugal pumps during power failure. *Renew. Energy* **2021**, *170*, 267–276. [[CrossRef](#)]
21. Li, X.; Tang, X.; Zhu, M.; Shi, X. 1D-3D coupling investigation of hydraulic transient for power-supply failure of centrifugal pump-pipe system. *J. Hydroinformatics* **2019**, *21*, 708–726. [[CrossRef](#)]
22. Tanaka, T.; Tsukamoto, H. Transient Behavior of a Cavitating Centrifugal Pump at Rapid Change in Operating Conditions—Part 2: Transient Phenomena at Pump Startup/Shutdown. *J. Fluids Eng.* **1999**, *121*, 850–856. [[CrossRef](#)]
23. Tsukamoto, H.; Matsunaga, S.; Yoneda, H.; Hata, S. Transient Characteristics of a Centrifugal Pump During Stopping Period. *J. Fluids Eng.* **1986**, *108*, 392–399. [[CrossRef](#)]
24. Zhang, Y.; Zhu, Z.; Li, W.; Xiao, J. Effects of viscosity on transient behavior of a low specific speed centrifugal pump in starting and stopping periods. *Int. J. Fluid Mech. Res.* **2018**, *45*, 1–20. [[CrossRef](#)]
25. Kan, K.; Zheng, Y.; Chen, H.; Zhou, D.; Dai, J.; Binama, M.; Yu, A. Numerical simulation of transient flow in a shaft extension tubular pump unit during runaway process caused by power failure. *Renew. Energy* **2020**, *154*, 1153–1164. [[CrossRef](#)]
26. Kan, K.; Chen, H.; Zheng, Y.; Zhou, D.; Binama, M.; Dai, J. Transient characteristics during power-off process in a shaft extension tubular pump by using a suitable numerical model. *Renew. Energy* **2021**, *164*, 109–121. [[CrossRef](#)]
27. Li, Z.; Bi, H.; Karney, B.; Wang, Z.; Yao, Z. Three-dimensional transient simulation of a prototype pump-turbine during normal turbine shutdown. *J. Hydraul. Res.* **2017**, *55*, 520–537. [[CrossRef](#)]
28. Ge, Z.; Feng, J.; Wu, Y.; Yang, Z.; Zhang, Y.; Zhu, G.; Luo, X. Numerical analysis on characteristics of transient process in centrifugal pumps during power failure under large flow initial condition. *Chin. J. Hydrodyn.* **2022**, *37*, 452–458. (In Chinese) [[CrossRef](#)]
29. Zhang, Y.; Zhu, Z.; Li, W.; Jia, X. Non-inertial stopping characteristics of a prototype pump. *Adv. Mech. Eng.* **2019**, *11*, 1687814019844649. [[CrossRef](#)]
30. Chen, S.; Jiang, H.; Zhou, Z.; He, Z.; Yan, D. Study on start-up transient process simulation of large scale tubular pumping stations. *J. Yangzhou Univ. Nat. Sci. Ed.* **2009**, *12*, 74–78. (In Chinese) [[CrossRef](#)]
31. Liu, M.; Han, Y.; Tan, L.; Lu, Y.; Ma, C.; Gou, J. Theoretical prediction model of transient performance for a mixed flow pump under fast start-up conditions. *J. Energy Storage* **2023**, *68*, 107678. [[CrossRef](#)]
32. Jin, F.; Luo, Y.; Bi, H.; Wang, H.; Wang, Z.; Lin, K.; Lei, X.; Yang, X. Transient simulation of reversible pump turbine during pump mode's starting up. *Phys. Fluids* **2023**, *35*, 025125. [[CrossRef](#)]

33. Long, Y.; Lin, B.; Fang, J.; Zhu, R.; Q. Fu. Research on the Transient Hydraulic Characteristics of Multistage Centrifugal Pump During Start-Up Process. *Front. Energy Res.* **2020**, *8*, 76. [[CrossRef](#)]
34. Li, Z.; Wu, P.; Wu, D.; Wang, L. Experimental and numerical study of transient flow in a centrifugal pump during startup. *J. Mech. Sci. Technol.* **2011**, *25*, 749–757. [[CrossRef](#)]
35. Fu, S.; Zheng, Y.; Kan, K.; Chen, H.; Han, X.; Liang, X.; Liu, H.; Tian, X. Numerical simulation and experimental study of transient characteristics in an axial flow pump during start-up. *Renew. Energy* **2020**, *146*, 1879–1887. [[CrossRef](#)]
36. Li, Q.; Ma, X.; Wu, P.; Yang, S.; Huang, B.; Wu, D. Study on the Transient Characteristics of the Centrifugal Pump during the Startup Period with Assisted Valve. *Processes* **2020**, *8*, 1241. [[CrossRef](#)]
37. Wang, Y.; Xie, L.; Chen, J.; Liu, H.; Luo, K.; Liu, Z.; Cao, M. Experimental Study on Transient Startup Characteristics of a Super Low Specific Speed Centrifugal Pump. *J. Chem. Eng. Jpn.* **2019**, *52*, 743–750. [[CrossRef](#)]
38. Shi, L.; Chai, Y.; Wang, L.; Xu, T.; Jiang, Y.; Xing, J.; Yan, B.; Chen, Y.; Han, Y. Numerical simulation and model test of the influence of guide vane angle on the performance of axial flow pump. *Phys. Fluids* **2023**, *35*, 015129. [[CrossRef](#)]
39. Liu, J.; Zheng, Y.; Zhou, D.; Mao, Y.; Zhang, L. Analysis of Basic Flow Pattern in Shaft Front-positioned and Shaft Rear-positioned Tubular Pump Systems. *J. Agric. Mach.* **2010**, *41*, 32–38. (In Chinese)
40. Deng, E.; Yue, H.; Ni, Y.; Wang, Y.; Xu, X.; Chen, Z. A turbulent crosswind simulation method at high-speed railway tunnel entrance: Based on field test and geometric turbulence generator. *Phys. Fluids* **2023**, *35*, 015156. [[CrossRef](#)]
41. Zhang, D.; Wu, S.; Shi, W.; Pan, D.; Yao, J.; Zhang, G. Application and experiment of different turbulence models for simulating tip leakage vortex in axial flow pump. *Trans. Chin. Soc. Agric. Eng.* **2013**, *29*, 46–53. (In Chinese) [[CrossRef](#)]
42. Menter, F. Review of the shear-stress transport turbulence model experience from an industrial perspective. *Int. J. Comput. Fluid Dyn.* **2009**, *23*, 305–316. [[CrossRef](#)]
43. Deng, E.; Yue, H.; Ni, Y.; He, X.; Yang, W.; Chen, Z. Wake dynamic characteristics of windproof structures in embankment–bridge sections along a high-speed railway under natural strong crosswinds. *Phys. Fluids* **2023**, *35*, 055109.
44. Kan, K.; Zhang, Q.; Xu, Z.; Chen, H.; Zheng, Y.; Zhou, D.; Binama, M. Study on a horizontal axial flow pump during runaway process with bidirectional operating conditions. *Sci. Rep.* **2021**, *11*, 21834. [[CrossRef](#)] [[PubMed](#)]
45. Chai, B.; Yang, J.; Wang, X.; Jiang, B. Pressure Fluctuation Characteristics Analysis of Centrifugal Pump as Turbine in Its Start-Up Process. *Actuators* **2022**, *11*, 132. [[CrossRef](#)]
46. Chen, S.; He, Z.; Zhou, Z.; Pan, G.; Yan, D. Study on transient process of low water-head large pumping station while pumping off. *J. Hydroelectr. Eng.* **2007**, *5*, 128–133. (In Chinese)
47. Jiao, H.; Chen, S.; Wang, M.; Liu, H. Comparison of transient characteristics of positive and negative power-off transition process of “S” shaped bi-directional full-flow pump. *Phys. Fluids* **2023**, *35*, 065113. [[CrossRef](#)]
48. Kan, K.; Xu, Z.; Chen, H.; Xu, H.; Zheng, Y.; Zhou, D.; Muhirwa, A.; Binama, B. Energy loss mechanisms of transition from pump mode to turbine mode of an axial-flow pump under bidirectional conditions. *Energy* **2022**, *257*, 124630. [[CrossRef](#)]
49. Yang, F.; Hu, W.; Li, C.; Liu, C.; Jin, Y. Computational study on the performance improvement of axial-flow pump by inlet guide vanes at part loads. *J. Mech. Sci. Technol.* **2020**, *34*, 4905–4915. [[CrossRef](#)]
50. Kan, K.; Zhang, Q.; Xu, Z.; Zheng, Y.; Gao, Q.; Shen, L. Energy loss mechanism due to tip leakage flow of axial flow pump as turbine under various operating conditions. *Energy* **2022**, *255*, 124532. [[CrossRef](#)]
51. Liu, J.; Liu, C. Modified normalized Rortex/vortex identification method. *Phys. Fluids* **2019**, *31*, 61704. [[CrossRef](#)]
52. Jiao, W.; Zhao, H.; Cheng, L.; Wang, Y. Numerical and experimental study on the hydrodynamic characteristics of the hub vortex at the nozzle of a water jet propulsion pump unit. *Phys. Fluids* **2023**, *35*, 065109.
53. Dong, X.; Gao, Y.; Liu, C. New normalized Rortex/vortex identification method. *Phys. Fluids* **2019**, *31*, 011701. [[CrossRef](#)]
54. Shu, Z.; Shi, G.; Dan, Y.; Wang, B.; Tan, X. Enstrophy dissipation of the tip leakage vortex in a multiphase pump. *Phys. Fluids* **2022**, *34*, 033310. [[CrossRef](#)]
55. Herwig, H.; Kock, F. Direct and indirect methods of calculating entropy generation rates in turbulent convective heat transfer problems. *Heat Mass Transf.* **2007**, *43*, 207–215. [[CrossRef](#)]
56. Kock, F.; Herwig, H. Local entropy production in turbulent shear flows: A high-reynolds number model with wall function. *Int. J. Heat Mass Transf.* **2004**, *47*, 2205–2215. [[CrossRef](#)]
57. Zhang, X.; Wang, Y.; Xu, X.; Wang, H. Energy conversion characteristic within impeller of low specific speed centrifugal pump. *Trans. Chin. Soc. Agric. Mach.* **2011**, *42*, 75–81. (In Chinese)

Disclaimer/Publisher’s Note: The statements, opinions and data contained in all publications are solely those of the individual author(s) and contributor(s) and not of MDPI and/or the editor(s). MDPI and/or the editor(s) disclaim responsibility for any injury to people or property resulting from any ideas, methods, instructions or products referred to in the content.